



HAL
open science

Turbulences

Nicolas Mordant

► **To cite this version:**

Nicolas Mordant. Turbulences. Data Analysis, Statistics and Probability [physics.data-an]. Ecole Normale Supérieure de Paris - ENS Paris, 2009. tel-00436459

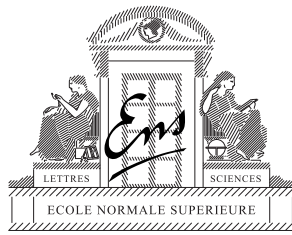
HAL Id: tel-00436459

<https://theses.hal.science/tel-00436459>

Submitted on 26 Nov 2009

HAL is a multi-disciplinary open access archive for the deposit and dissemination of scientific research documents, whether they are published or not. The documents may come from teaching and research institutions in France or abroad, or from public or private research centers.

L'archive ouverte pluridisciplinaire **HAL**, est destinée au dépôt et à la diffusion de documents scientifiques de niveau recherche, publiés ou non, émanant des établissements d'enseignement et de recherche français ou étrangers, des laboratoires publics ou privés.

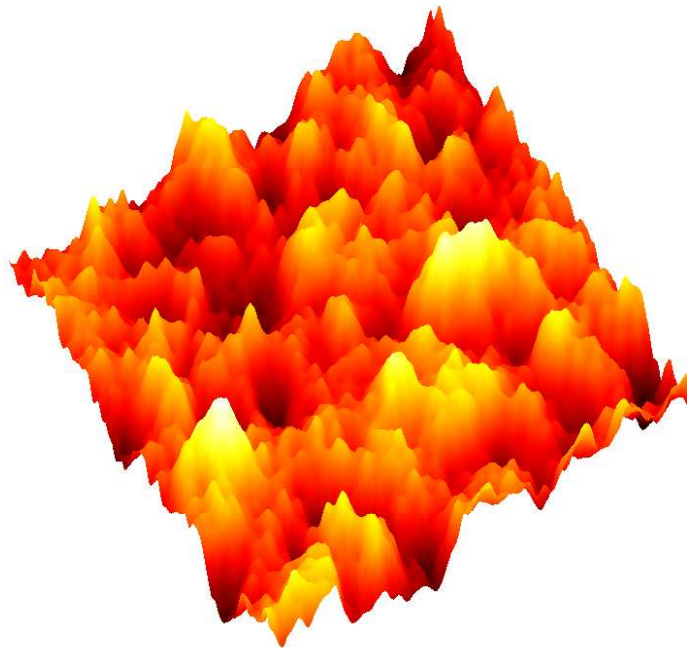


HABILITATION À DIRIGER DES RECHERCHES

Turbulences

Nicolas MORDANT

2009



DÉPARTEMENT DE PHYSIQUE
LABORATOIRE DE PHYSIQUE STATISTIQUE

Introduction

A turbulent flow can be viewed as a nonlinear system out of thermodynamical equilibrium: it is canonically forced in a narrow range of scales (length or time scales) and energy is transferred through nonlinear interactions to a wide continuous range of time and length scales. In the case of 3D hydrodynamical turbulence, energy cascades down scales until scales are small enough so that dissipation dominates and pumps energy from the flow into heat. The same phenomenology occurs for wave turbulence with the additional space-time relation provided by the dispersion relation inherent to the waves. The deterministic equations of motion are known (the Navier-Stokes equations or the nonlinear wave equation) but for hydrodynamics, solutions resist the theoretical investigations so far. Statistical theories are looked for to deal with the observed stochasticity of the motion.

The ultimate goal of the physicist is to exhibit some universality in turbulence statistics. This would yield to models intended to simulate practical situations which have inherently specific forcing conditions. For instance Large Eddy Simulations rely on the statistical modeling of the small scales of turbulence which are believed (hoped ?) to be universal to a large extent. Nevertheless, so far no fully satisfactory sub-grid modeling has been implemented. Among the variety of sub-grid models, one can cite Eulerian-Lagrangian schemes which sub-grid models simulate the stochastic motion of particles advected by the small scale flow. The experimental study of the behavior of such particles has seen huge progress in the last decade. In this period, several experimental techniques have been developed to track particles in turbulent flows. Fluid particles, or Lagrangian particles, are tracers of the flow. The properties of their motion is intimately related to the transport properties of the flow: a passive concentration field (or passive scalar) which does not contribute to the dynamics of the flow is carried by fluid particles (with some additional molecular diffusion). For high Reynolds and Péclet numbers the dispersion of the scalar is dominated by the advection by the turbulent motion. Thus the evolution of the concentration field is directly related to the properties of the motion of fluid particles. The motion of particles, bubbles or droplets in turbulent flows is also of interest in practical issues such as aerosol transport, cloud dynamics, chemical reactors, sedimentation, erosion...

Similarly to the link between concentration dynamics and particle motion, the evolution of the magnetic field at large magnetic Reynolds number is intimately related to the Lagrangian evolution of material lines in electrically conducting fluids. Being a vector, the magnetic field can be amplified by the motion of the flow in contrast to scalar concentration. If a sustained amplification of a trace magnetic field can be reached, it leads to dynamo action. This phenomenon is at the origin of the magnetic field of such astrophysical objects as planets, stars or galaxies. Indeed a large scale magnetic field is generated from the turbulent motion of a conducting fluid such as the molten iron core of the Earth.

If the general idea of fluid dynamo action was introduced about a century ago by Larmor, the mechanism for magnetic field generation from turbulent motion is not known in great details. Some mechanisms based on laminar motions have been proposed and tested experimentally. A mean field process has been proposed but the usual lack of scale separation in turbulent motion tend to invalidate it [29]. The question of the role of the average large scale motion as opposed to that of the turbulent fluctuations is still debated especially for experiments using liquid metals. In these cases, the magnetic Reynolds number is usually not very high and the kinetic Reynolds number is several orders of magnitude higher. The Von Kármán Sodium (VKS) experiment was designed to get some insight on these issues. It is a fully turbulent weakly constraint sodium flow which reached dynamo action. It was also successful in generating a variety of dynamical regimes (reversals, oscillations) sharing some similarity with the behavior of the terrestrial or solar magnetic fields.

Wave turbulence shares many phenomenological similarities with hydrodynamical turbulence. The same wide spectrum of scales and out of equilibrium energy fluxes can be observed. The main difference lies in the fact that a statistical theory of wave turbulence exists in the case of small non linearity: the Weak Turbulence Theory (WTT). It also exhibits a Kolmogorov energy cascade and in some cases inverse cascades. Due to the weak non linearity approximation many statistical quantities can be computed an-

alytically and possibly compared to experiments. Even though the general WTT was developed in the 60-70's, well controlled laboratory experiments were designed mostly in the past decade and concern mainly fluid surface waves (gravity of capillary waves). Lately Düring, Rica & Josserand applied the WTT to elastic thin plates. They compared theory and numerical simulations and the thin plates appear as good candidates to study wave turbulence experimentally.

My personal contribution to the investigation of these issues was mostly experimental and usually in close collaboration with theoreticians. Concerning the study of particles in turbulent flows I developed a Doppler technique based either on ultrasound or laser to track the velocity field of single particles. I also took part in the development of a 3D high speed imaging technique to track particles. These new original measurements shed some new light on turbulence studies, in particular on the issue of intermittency in hydrodynamical turbulence. During the PhD of Michaël Berhanu, we developed a new gallium experiment and studied in particular the influence of a strong magnetic field on the statistical properties of the turbulent fluctuations of the flow. This question is related to the saturation of the growth of the dynamo magnetic field. I also belong to the VKS collaboration in which I take part in the data acquisition and analysis. More recently I developed a new experiment aimed at studying wave turbulence in a thin elastic steel plate. I will review in the following my contributions to these issues.

This article is a synthesis of my personal research work and not a full bibliographical record of the latest work in each field. The “References” section lists only selected references useful in the perspective of my own work. For a more general view, the reader should refer to reference sections of the cited articles. Most figures are extracted from my published articles. Due to the limited space available only the main features are described. The reader is invited to refer to the original articles for the full details on the experimental configurations.

1 Particles and hydrodynamical turbulence

Since 1998, a large part of my research activity is dedicated to the experimental study of the dynamics of small solid spheres advected by a turbulent flow. In this section, I will first recall briefly the general framework of the modeling of the behavior of particles in a flow. Then I present the Doppler techniques I developed in Lyon with J.-F. Pinton during my PhD and later with R. Volk. I describe also the optical tracking technique I used in Cornell University with A. Crawford and E. Bodenschatz. Then the experimental observations of the dynamics of tracer and inertial particles are presented. The experimental observations are often compared to numerical simulations by E. Lévêque or by E. Calzavarini & F. Toschi. In particular, for inertial particles, the experiments allowed us to improve the modeling of the particle in the numerics. The emphasis is then placed on intermittency. Collaborations with A. Arnéodo, J. Delour, S. Roux and L. Chevillard were very fruitful in the understanding of the origin of intermittency in the Lagrangian framework. Finally I will show very recent experimental results of scalar dispersion in relation to the dynamics of tracer particles.

1.1 Modeling the dynamics of a particle in a flow

When the density of the particles is matched with that of the fluid and the diameter is small, it is expected that the particles behave as tracers and reflect the motion of the fluid particles. The study of tracer particles gives access to the dynamics of the Lagrangian velocity i.e. the velocity of the particle along its motion in time. When the density is not matched and/or the size is not infinitely small, then the dynamics of the particle can be quite different from that of the fluid due to inertia.

A large variety of models exist to describe the motion of particles in a flow. Depending on whether the flow is known or has to be also modeled, two classes of approach exist. First I describe a deterministic model which is aimed at describing the difference in behavior between inertial and tracer particles. Ingredients of this model are used in particular in numerical simulations of the motion of inertial particles.

Then I recall a very simple Langevin stochastic model for the motion of tracer particles. Modifications to this basic model will be introduced later to take into account the experimental observations.

To simulate the motion of a small particle in a known flow, a deterministic approach can be used to compute the hydrodynamical forces acting on the particle. The usual starting point is the Maxey & Riley equation [28] for a small particle in the case of a particle Reynolds number Re_p going to zero. By computing the perturbation to the base flow due to the presence of the particle, Maxey & Riley end up with the following evolution equation of the particle velocity \mathbf{v}_p :

$$m_p \frac{d\mathbf{v}_p}{dt} = (m_p - m_f)\mathbf{g} + m_f \frac{Du}{Dt} + 6\pi a \mu_f (\mathbf{u} - \mathbf{v}_p) + \frac{1}{2} m_f \frac{d(\mathbf{u} - \mathbf{v}_p)}{dt} + 6a^2 (\pi \mu_f \rho_f)^{1/2} \int_0^t \frac{d(\mathbf{u} - \mathbf{v}_p)}{dt} \frac{1}{(t - \tau)^{1/2}} d\tau \quad (1)$$

where m_p and m_f are the mass of the particle and the mass of the same volume of fluid, \mathbf{g} is the gravity acceleration, μ_f is the viscosity, a is the particle radius, ρ_f is the fluid specific gravity, u is the unperturbed flow velocity at the same position. The successive terms of the right hand side (rhs) of (1) are: the buoyancy, the Lagrangian acceleration of the fluid at the same position, the Stokes drag, the added mass contribution and last the Basset history term. Several modifications can be introduced to take into account larger Reynolds numbers [33]. The Stokes drag must be taken non linear for instance. The Basset history term is due to the diffusion of the vorticity away from the sphere and is non local in time. Its expression is valid only at zero Re_p and for non zero Re_p it is only partially known [33]. The simplest case is that of infinitely heavy and infinitely small particles: the only remaining term is the Stokes drag which incorporates a finite response time of the particle to the fluid action. This is most likely valid for aerosol particles in the atmosphere but most particles used in experiments do not match these conditions. As soon as the size is not infinitely small other terms should be taken into account. The first correction could be the added mass term yielding

$$\frac{d\mathbf{v}_p}{dt} = \beta \frac{Du}{Dt} + \frac{1}{\tau_p} (\mathbf{u} - \mathbf{v}_p) \quad (2)$$

with $\beta = 3\rho_f/(\rho_f + 2\rho_p)$ (ρ_p is the particle density) and $\tau_p = a^2/(3\beta\nu)$ ($\nu = \mu_f/\rho_f$ is the kinetic viscosity). This equation incorporates both finite time response and density effects. It is used in numerical simulations but is seen not to reproduce the experiments, in particular not to take correctly into account the size effects at given density [60].

In the case of tracer particles, the motion of the particle can be modeled without simulating the whole flow by using the formalism of the Langevin equation. The turbulent flow is modeled stochastically:

$$dv_p = -\frac{v_p}{T_L} dt + \sqrt{C_0 \epsilon} dW, \quad (3)$$

where v is a component of the Lagrangian velocity, ϵ is the dissipation rate, C_0 is a dimensionless parameter, $T_L = \frac{2\sigma^2}{C_0\epsilon}$ is the Lagrangian time (σ^2 is the velocity variance) and dW is a Wiener process. This is the simplest version which is in agreement with the scaling predictions of the Kolmogorov 1941 theory for homogeneous and isotropic turbulence. In this case C_0 is the only parameter. Its value is expected to be close to 4 from our measurements [39]. Several modifications of this equation can be introduced to take into account finite Reynolds number effects or intermittency corrections (see [53, 55] for instance).

1.2 Tracking particles in a turbulent flow

The experimental difficulty of particle tracking in turbulence flows lies in the large spectrum of time and length scales typical of turbulent flows that has to be resolved. Imaging tracking techniques record the position of the particles and thus have to resolve both space and time scales. In contrast, Doppler techniques provide only the velocity of a single particle but only the time scales have to be resolved. I contributed to the development of both kind of techniques which distinct advantages are complementary.

All my studies of the Lagrangian statistics of turbulence have been conducted in various configurations of Von Kármán flows i.e. the flow generated by counter rotating disks (see [40, 37, 61] and references therein). Von Kármán flows are convenient because the flow is closed, of moderate size and highly turbulent in contrast to wind tunnels for instance. As all my data share the same geometry, it makes comparison straightforward. All measurements were performed in the central region of the Von Kármán flow where turbulence is the closest to homogeneity and isotropy.

1.2.1 Doppler tracking techniques

Doppler techniques are based on the tracking of the frequency shift of a wave scattered by a moving solid particle. Ultrasound or light can be used [40, 61, 60]. The difficulty of the frequency demodulation restricts the technique to the measurement of the time evolution of the velocity of a single particle. Ultrasound and light have distinct advantages. It is easy to make wide ultrasonic beams so as to investigate large volumes and the piezoelectric transducers are cheap and have a very high sensitivity. The main drawback of ultrasound is the restriction to fairly large particle sizes (250 μm which may not behave fully as tracer particle) due to the strong drop in the scattering cross section for sub-wavelength particles. In contrast, the Laser Doppler technique achieves a very good time resolution and can track particles that are a few microns in diameter. The limitation in our implementation is mainly the size of the beam (about 1/10-th of the ultrasonic beam) and the sensitivity of the photomultiplier. I developed the ultrasonic method during my PhD with J.-F. Pinton and the Laser technique in collaboration with R. Volk.

The time resolution achieved for both techniques relies on a high performance Approximated Maximum Likelihood (AML) demodulation scheme developed in collaboration with Olivier Michel [42, 41]. This method is parametric: it assumes that the measured signal is made of a frequency modulated sine component (with a slowly varying amplitude) corresponding to the particle and some white gaussian noise. These ingredients are incorporated into a generic AML spectral estimation method embedded in a Kalman filter which achieves a temporal tracking of the Doppler frequency shift. This scheme makes this method more efficient than Fourier-based time frequency methods both for the time resolution and the computing time. It is the core of the performance of the Doppler technique.

Ultrasound Doppler and Laser Doppler are quite complementary. The former gave access for the first time to time scales in the inertial range up to the Lagrangian integral time scale thanks to the wide measurement volume. The latter technique enabled us to measure the acceleration and to resolve dissipative scales for various kinds of particles.

1.2.2 Ultrafast imaging technique

Imaging techniques are the most common techniques for particle tracking. A region of the flow is illuminated and viewed from several angles by multiple cameras. The position of the particles can be reconstructed from the movies and tracked in time. The major technical difficulty lies in the constraint to resolve both time and length scales of the turbulent flow. For example, in a typical laboratory water flow at high Reynolds number the length scales range from a few tens microns to a couple centimeters and time scales from sub millisecond to a tenth of a second. It requires then both high speed and a large number of pixels. Only a partial range of scales can usually be resolved depending on the technical choices. At Cornell University, we used silicon strip detectors whose main advantage is their very high speed: 70000 frames per second. They are linear sensors with at most 512 pixels which restricts the performance to dissipative length scales and only a couple particles viewed at the same time. The high recording rate allowed us to study in details the statistics of acceleration [17, 37]. The method preexisted my arrival at Cornell but I extended the system so that the full 3D acceleration could be measured by doubling the number of available detectors. I worked in close collaboration with A. Crawford during her last years of graduate student at Cornell.

Laser Doppler and Silicon strip detectors achieve the same resolution and have been in this way validated against each other [61]. Both techniques are limited to a single or a few particles measured

at the same time. These two techniques allowed to study acceleration statistics at the highest Reynolds number.

1.3 Dynamics of a fluid particle in a turbulent flow

1.3.1 Tracer particles

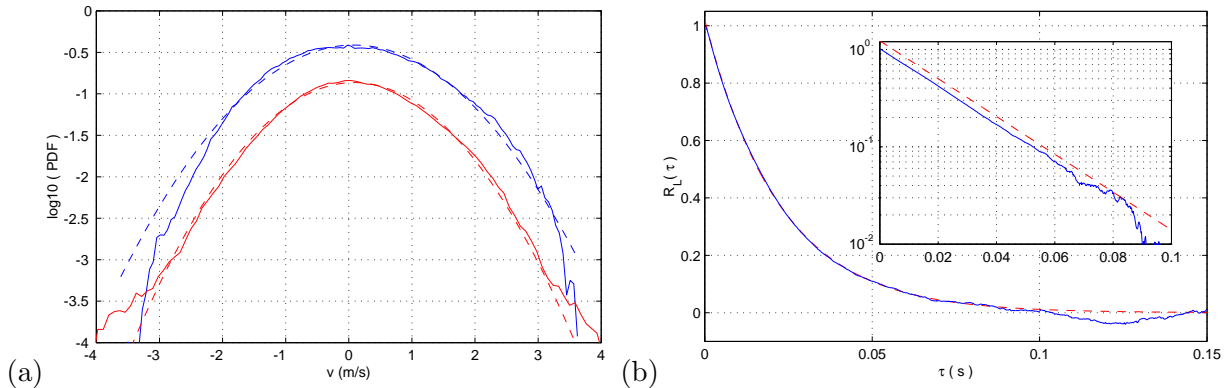


Figure 1: Statistics of the Lagrangian velocity of a fluid particle at $R_\lambda \approx 800$ measured by ultrasound Doppler. (a) PDF of two component of the velocity. The two PDFs have been shifted for clarity. Dashed lines are gaussian distribution with the same variance. (b) Autocorrelation of one component of the velocity. The dashed line is an exponential fit. Figures from [33].

As seen in figure 1, the distribution of the Lagrangian velocity components is Gaussian [40] as expected from the Eulerian measurements (in homogeneous and isotropic turbulence, both distributions are expected to be identical). The time autocorrelation $R_L(\tau) = \langle v(t + \tau)v(t) \rangle$ (along a single particle trajectory) is decaying exponentially at long times [40]. These observations seem to validate the modeling of the Lagrangian velocity by a Langevin equation (3). A closer analysis of the small time scales by studying the correlation of the acceleration components (figure 2) shows that the existence of a short time scale which scales with the Kolmogorov time scale τ_η as confirmed by comparing the experimental data to DNS by E. L ev eque in particular [39, 37]. This supports Langevin modeling of acceleration rather than velocity so as to take into account the finite Reynolds number [55].

From figure 2, it can be seen that the decay of the correlation of the magnitude of acceleration is slower than that of the component. This can be understood dynamically by the existence of intense filaments of vorticity. Fluid particles can be trapped in these structures for long times as these structures are long lived with lifetimes of the order of the integral time scale. In that case the acceleration magnitude can remain correlated for long times, as long as the particle is circling in the vortex. The Sawford model [55] of a simple second order Langevin equation does not reproduce these long time correlations. Incorporating them in such a model has been attempted and is related to intermittency issues as discussed below.

1.3.2 Inertial particles

The study of tracer particles provides some information on the flow itself. It is also of interest to study the dynamics of inertial particles to get some more insight on the flow but also to get some information on the transport properties of multiphase flows. These flows are present in environmental (clouds) or industrial (reactors) situations for instance.

If the density of the particle is not matched with that of the fluid, then two main effects impact the dynamics of the particle. First, the particle inertia is different from that of the fluid so that heavier particles are slower to react or on the contrary, bubbles for example can be faster [60, 61]. Second, the particles behave differently in regions of the flow with high vorticity. Heavier particles tend to be expelled from vortices whereas lighter particles are attracted into the core of the vortices. In this way, various kinds of particles sample different regions of the flow: heavy particles tend to favor high strain regions while lighter particles favor vortical regions. As seen in figure 3, this impacts the dynamics of

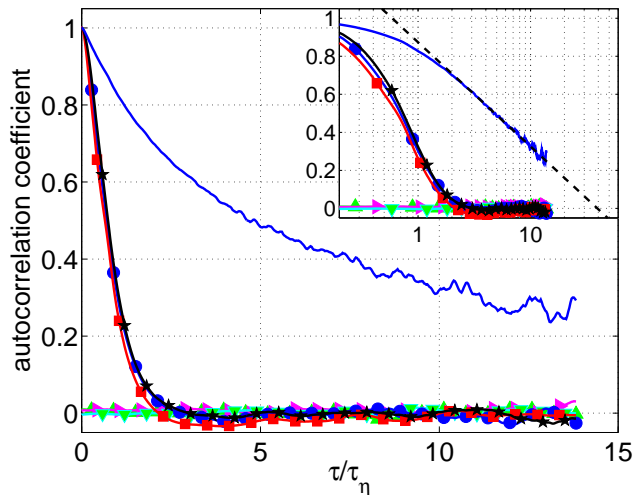


Figure 2: Correlation of the acceleration components at $R_\lambda \approx 700$ measured with the silicon strip detectors. Squares, circles and stars: autocorrelation of the three acceleration components. Triangles: crosscorrelation of components. Solid line: autocorrelation of the magnitude of the acceleration. Insert: same in semilog scale. Figure from [37].

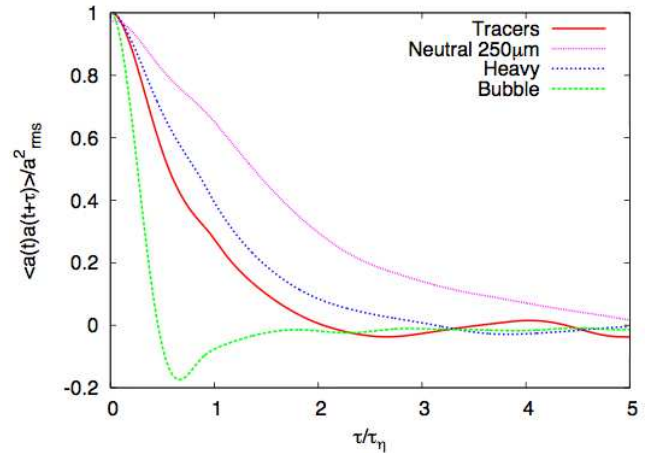


Figure 3: Autocorrelation of a component of the acceleration of inertial particles in water. “Tracers” are density matched $15 \mu\text{m}$ (radius) particles, “neutral” are density matched $125 \mu\text{m}$ particles, “heavy” are density 1.4, $20 \mu\text{m}$ particles and “bubbles” are air bubbles of size about $75 \mu\text{m}$. See [60] for details.

the particles at short time scales. Size effects can also change the dynamics as larger particles tend to be sensitive to a spatially averaged flow over their size [39, 60]. Taking these effects into account in numerical simulations is not straightforward but attempts are underway [60, 9]: our experimental data was compared with numerical simulations by E. Calzavarini & F. Toschi. It showed in particular that taking into account the added mass term as in eq. (2) was necessary to reproduce the influence of density. It was nevertheless not enough to take into account the size effects of large, density matched particles. R. Volk is currently performing an extensive analysis of these effects using the Laser Doppler technique.

1.4 Intermittency

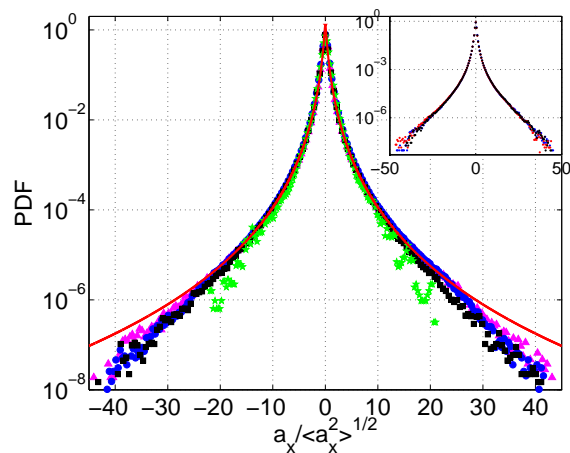


Figure 4: Centered distribution of the acceleration components at $R_\lambda = 285$ (green), 485 (black), 690 (blue), 970 (pink). Insert: centered PDF of the three acceleration components at $R_\lambda = 690$. Solid line: model of PDF assuming a lognormal distribution of the acceleration magnitude of variance 1. Data measured with the silicon strip detectors. Same data as [37].

So far our observations seem to support the modeling of the tracer particles by a simple second order Langevin equation. In that case all the statistics would be gaussian. But the striking feature related to

the Lagrangian acceleration is the extremely wide distribution of its components (figure 4(a)). Extremely high acceleration values have been recorded (e.g. 16000 m.s^{-2} in Cornell University [48]). Events as large as 40 times the rms acceleration have been readily observed which would have been impossible to record if the distribution would be Gaussian. The distribution is so wide that the existence of the flatness was questioned [36]. The question is not fully answered as values of the flatness up to 100 have been estimated [37]. We confirmed the shape of the acceleration PDF initially observed at Cornell University by an independent Laser Doppler measurement in a similar Von Kármán flow [61].

1.4.1 Intermittency of the Lagrangian velocity field

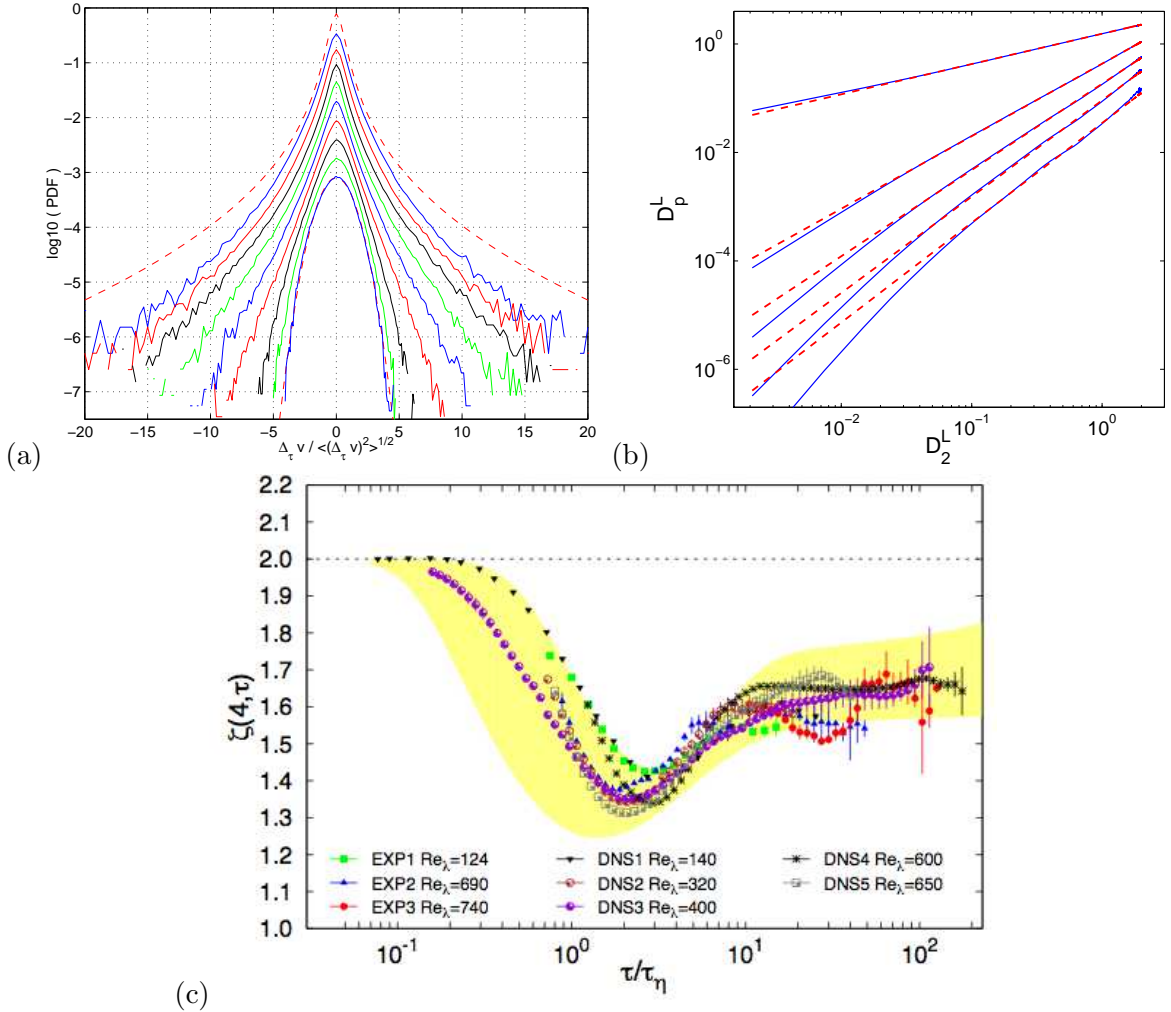


Figure 5: (a) Distributions of the velocity increments $\Delta_\tau v$. Solid lines: PDF of the increments for $\tau = 0.15, 0.31, 0.61, 1.2, 2.5, 4.9, 9.8, 20$ at 39 ms (from top to bottom). At $R_\lambda \sim 800$, we measured $T_L \approx 22$ ms. Data from ultrasound Doppler. Top dashed line: PDF of the acceleration component measured by silicon strip detectors from [48]. Bottom dashed line: Gaussian distribution. Figure from [33]. (b) ESS plot of the structure functions $S_p(\tau)$ (here noted D_p) versus $S_2(\tau)$ for $p = 1, 3, 4, 5, 6$ from top to bottom together with linear fits in dashed line. The estimated slopes are $\zeta_p = 0.56, 1.34, 1.58, 1.76, 1.9$ respectively. Figure from [39]. (c) Compilation of experimental and numerical values of the scale dependant fourth order scaling exponent $\zeta(4, \tau)$ of $S_4(\tau)$. Our ultrasound Doppler data is EXP3. Details about other datasets are to be found in [2]. The yellow area is the prediction obtained starting from Eulerian measurement through a change of variable from length scale to time scale in a multifractal framework. Figure from [2].

If the statistics of the velocity increments $\Delta_\tau v = v(t+\tau) - v(t)$ is scale invariant, then the distribution of the increments should be gaussian at all scales (as it is Gaussian at large scale). Acceleration is an increment for τ going to zero and is strongly non Gaussian thus scale invariance is broken. This feature is

called intermittency. It is similar to what is observed for spatial increments for Eulerian measurements. One way to make this statement quantitative is to study the evolution of the successive moments of the velocity increments as a function of the time scale. Structure functions are defined in our case as $S_p(\tau) = \langle |\Delta_\tau v|^p \rangle$ with absolute values as the distribution of the increments is symmetrical. The structure functions are assumed to behave as power laws $S_p(\tau) \propto \tau^{\zeta_p}$. Scale invariance would lead to $\zeta_p = p/2$ following the Kolmogorov 1941 theory.

The experimental distribution of the increments are shown in figure 5(a) together with the structure functions in (b). The shape of the PDF is seen to be varying with scale meaning that the exponents ζ_p are lower than $p/2$. Figure 5 displays a compilation of several datasets from experiments or numerical simulations for the exponent $\zeta(4, \tau)$ defined as the scale dependent logarithmic slope of $S_4(\tau)$. All data sets are collapsing fairly well including in the dissipative range. This suggests some universality of the Lagrangian intermittency.

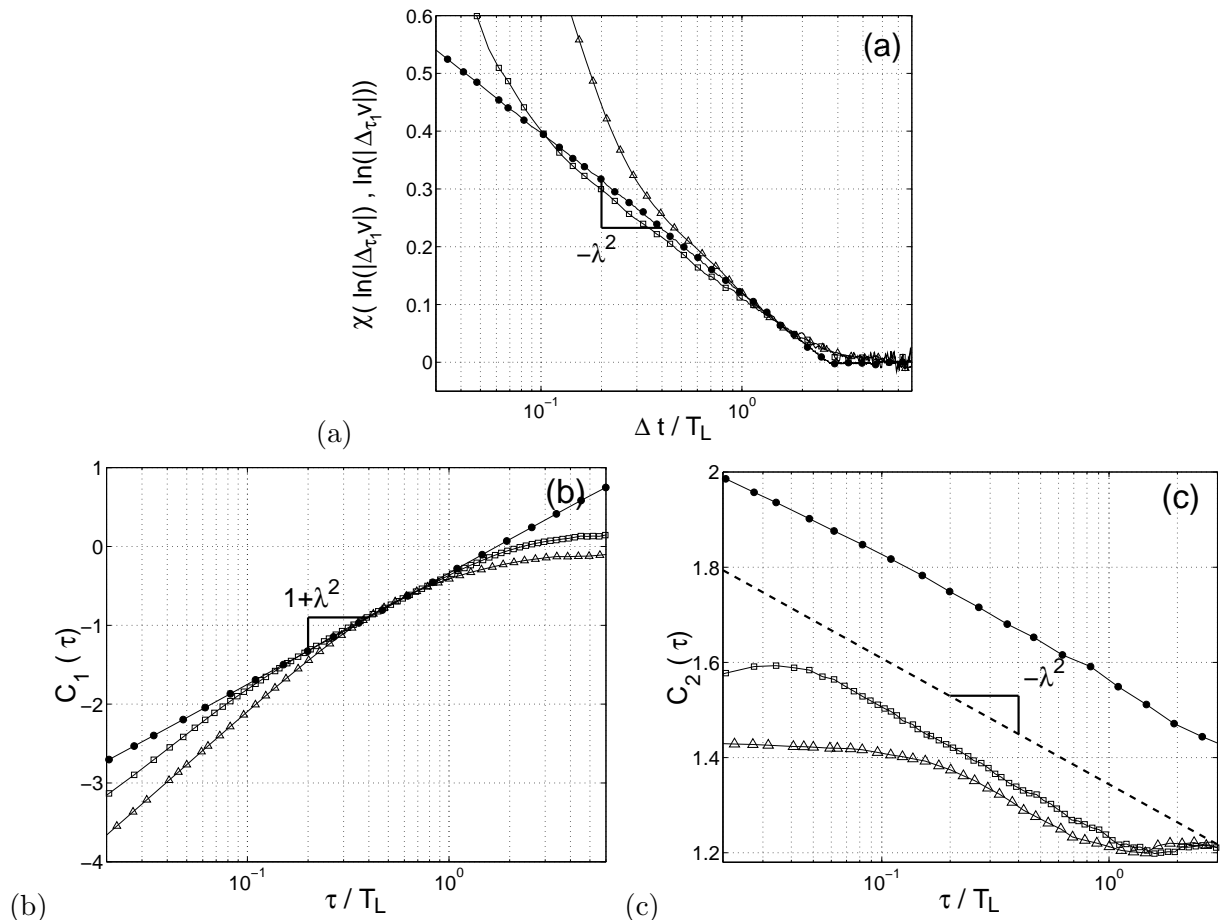


Figure 6: (a) Correlation of the log of the magnitude of the velocity increments. (b) First cumulant, (c) second cumulant. Data at R_λ close to 800 from ultrasound measurement (squares), data from DNS at $R_\lambda = 70$ (triangles) and MRW model (dots). From [38].

Our observations confirmed that the simple Langevin model for tracer particles had to be modified. The origin of the intermittency properties can be related to the long correlations of the acceleration magnitude. The model of multifractal random walk (MRW), developed by J. Delour during his PhD, incorporates the long correlations to recover the intermittent scaling properties of the inertial range [38]. Instead of using a Wiener process as the stochastic force in the Langevin equation (3), the stochastic force is taken as the product of a white noise by an amplitude $A(t) = \exp \omega(t)$. ω is gaussian and its correlations are chosen so that

$$\langle \omega(t) \omega(t + \tau) \rangle = -\lambda^2 \ln(\tau/T_L). \quad (4)$$

The models predicts that the cumulants of the velocity increments should behave as

$$C_1(\tau) = (1 + \lambda^2) \ln \tau, \quad C_2(\tau) = -\lambda^2 \ln \tau \quad (5)$$

In figure 6(a), we show the decay of the correlation of the logarithm of the velocity increments compared with the MRW model with $\lambda^2 = 0.115$. The observed decay is fairly logarithmic. Figure 6(b,c) show the evolution of the first two cumulants. The slope of both cumulant is reproduced with the same value of λ^2 as predicted by the model (even if a vertical shift is observed for C_2). This strongly suggests that the MRW captures the main feature of intermittency in the inertial range.

In the same spirit, models inspired by non extensive statistical mechanics have been proposed to reproduce the wide tails of the acceleration PDF. The most convincing was proposed by C. Beck [4] and extended by A. M. Reynolds [53] to model the full range of time scales. A second order stochastic model for the acceleration is coupled to a second stochastic equation for the dissipation rate which distribution is lognormal with a characteristic time close to the integral Lagrangian time. With A. M. Reynolds, we compared his model to our acceleration data [54]. His model reproduces both the distribution of the acceleration components and the intermittency properties of the inertial range.

1.4.2 Relating Eulerian and Lagrangian intermittencies

A more detailed way to describe intermittency is through the multifractal formalism as proposed by L. Chevillard *et al.* [11]. This is not an attempt to build a dynamical model but rather to provide an accurate and quantitative description of the statistical properties of the velocity field. The originality of the method is to incorporate also the dissipative range into the description. The velocity increments are written as

$$\Delta_\tau v = \beta(\tau/T_L) \delta_{T_L} v \quad (6)$$

where all the time scale dependance is contained in the random function β (the integral scale increment $\delta_{T_L} v$ is gaussian). In the multifractal formalism, β has a power law dependence in the inertial range $\beta \sim (\tau/T_L)^h$ with a spectrum $\mathcal{D}(h)$ (i.e. the PDF \mathcal{P}_i of observing an exponent h at scale τ is proportional to $(\tau/T_L)^{1-\mathcal{D}(h)}$). In order to incorporate the dissipative range different properties of the scaling of β and of the distribution $\mathcal{P}(h)$ have to be imposed in the dissipative or the inertial regime. In the dissipative range, $\beta \sim (\tau/T_L)$ and $\mathcal{P}_d(\beta) \sim (\tau_\eta(h)/T_L)^{1-\mathcal{D}(h)}$. The crossover between the two regimes corresponds to a local Reynolds number equal to one. With this definition the crossover h^* of the exponent h between the two regimes corresponds to $h^*(\tau/T_L, Re) = -\frac{1}{2} \left(1 + \frac{\ln Re}{\ln \tau/T_L} \right)$ with an explicit dependence on the integral scale T_L and in the Reynolds number. The PDF of the $\Delta_\tau v$ is then the sum over the exponents h of the contributions of the dissipative and the inertial ranges. The function β is then a function of h , τ/T_L and Re . An interpolating function for β is proposed in order to interpolate smoothly between the two regimes. With this formalism, it is possible to fit our experimental data (ultrasound Doppler and silicon strip detectors) for the PDF of velocity increments to extract the singularity spectrum $\mathcal{D}(h)$ which contains all the information on the intermittency properties. A analytical formulation of $\mathcal{D}(h)$ is prescribed and taken as a quadratic form as a lowest order approximation: $\mathcal{D}(h) = 1 - (h - c_1)^2/2c_2$.

Figure 7(α) shows the quality of the fit by the multifractal procedure and figure 7(β) displays the corresponding spectrum $\mathcal{D}(h)$. It is to be noted that the experimental data comes from two different experiments and the DNS is performed at a much lower Reynolds number. Nevertheless the extracted $\mathcal{D}(h)$ are extremely close to each other suggesting some universality and no dependence of the spectrum in the Reynolds number.

The multifractal framework has been extensively applied to the Eulerian statistics [22] providing an equivalent Eulerian spectrum of exponents $\mathcal{D}^E(h)$. Both spectra can be related by

$$\mathcal{D}(h) = -h + (1 + h)\mathcal{D}^E(h/(1 + h)). \quad (7)$$

The standard models of the Eulerian multifractal description provide the two thin lines in figure 7(β). It can be seen that the lower part of the Lagrangian spectra is very well reproduced but some disagreement is observed for the highest exponents. This could be an artifact of the fitting procedure as for instance

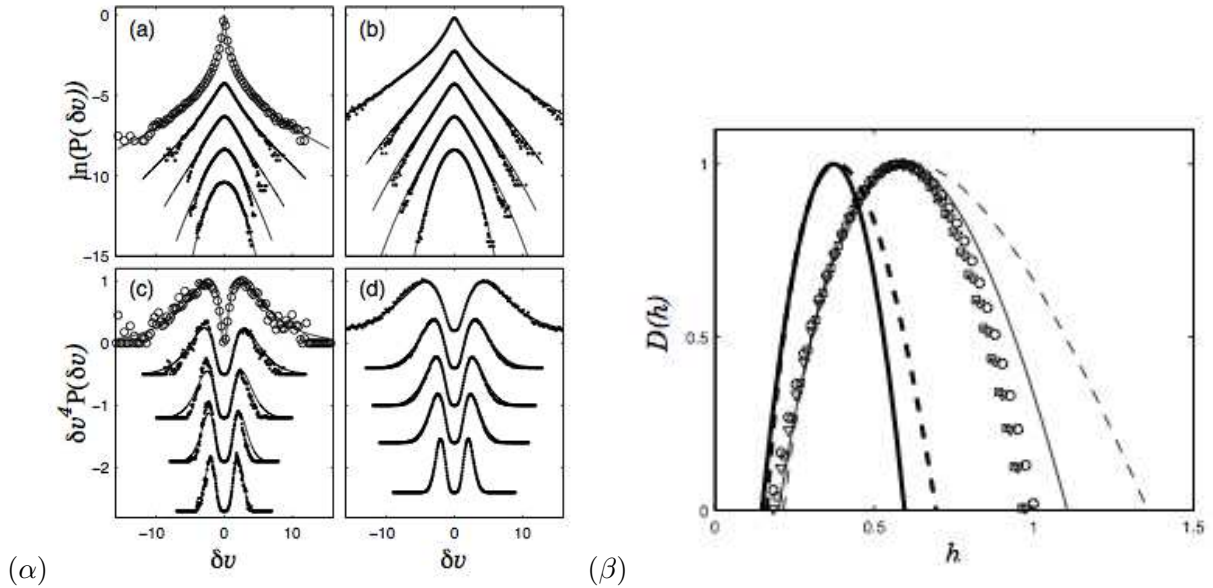


Figure 7: (α) (a)(c) Fit of the multifractal description on experimental data (circles: acceleration data from Cornell, dots: velocity increments from ultrasound Doppler, solid lines fits) – (b)(d) same for numerical simulations. See [11] for details. (β) Spectrum $\mathcal{D}(h)$ extracted from the silicon strip acceleration data (triangles), ultrasound data (squares) and DNS data (circles). Thick lines are Eulerian spectra (lognormal: solid, log-Poisson: dashed) and thin lines are their Lagrangian counterparts. Figures from [11].

the Lagrangian and Eulerian spectra can not be simultaneously log-normal from the above formula. The shaded area in figure 5(c) corresponds to the computation of the fourth order structure function exponent from this translation from Eulerian to Lagrangian in the same range of Reynolds numbers as the data represented. It can be seen again that this translation is quite efficient at reproducing the Lagrangian data.

Relating this multifractal description to the previous dynamical observations is not a straightforward task and remains an open problem. Nevertheless the following test can be performed: we advected particles in a frozen snapshot of a turbulent velocity field. The scaling properties of the Eulerian field are present but the time variability is lost. The intermittency exponents are similar to that of the Eulerian field and not to that of the Lagrangian field [12]. It confirms that the time dynamics of the flow is a key ingredient and the occurrence of long time correlations is a prime feature.

1.4.3 Inertial particles and polymer solutions

One way to change slightly the dynamics of the particles can be either to change their inertia or to change the properties of the fluid. To change inertia, it is possible to use other materials such as glass, metals, air (bubbles) or simply to change the size of the particle [60, 61]. As reported above, all this changes the time scales of the particle dynamics. To change the properties of the fluid, one can use dilute polymer solutions [18]. Adding polymer in tiny concentrations does not alter the shear viscosity but changes by several orders of magnitude the elongational viscosity. Purely elongational flows are almost suppressed. This should modify in particular the stretching regions of the flow. These regions are of importance to sustain highly vortical structures such as vorticity filaments. As we suggested above, altering the dynamics may change the intermittency properties.

In the case of polymers, the dynamics of the particle trajectories is indeed altered as can be seen in figure 8(a). First the acceleration variance is strongly reduced when adding a small fraction of polymer and second the characteristic time is increased. Figure 8(b) shows the acceleration distribution for pure water and for a polymer solution. No strong change of the distribution is observed [18]. More recent measurements from the Bodenschatz group have shown that the cascading process is strongly altered by the addition of polymer [45]. The energy transfer is modified but not the distribution of acceleration.

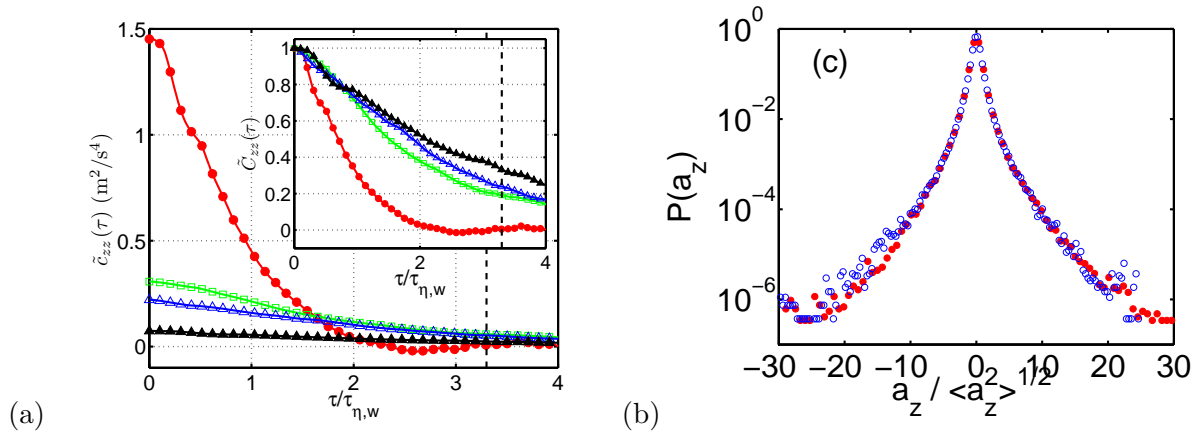


Figure 8: (a) Autocovariance of one acceleration components for various concentration of polymer PAA at $R_\lambda = 285$. From top to bottom: pure water, 3.5 ppm, 5 ppm and 10 ppm. Insert: autocorrelations. (b) Comparison of the distribution of the acceleration component. Blue: water, red: 5 ppm solution. Data from silicon strip detectors. Figures from [18].

A detailed multifractal analysis of the polymer datasets should be performed to give a more precise description of the possible modification of the intermittent properties of the Lagrangian velocity.

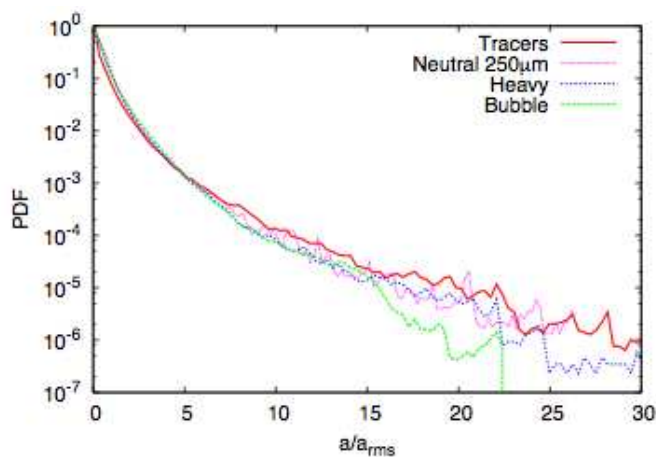


Figure 9: Comparison of the distribution of the acceleration component for various particles: tracers, large neutrally buoyant particles, heavy particles (density 1.4) and bubbles. Data from Laser Doppler. Figure from [60].

In the case of inertial particles, we observe also that even though the dynamics is modified, the acceleration distribution is unchanged (figure 9) [60, 61]. Similar results have been reported for wind tunnel data by M. Bourgoin and coworkers [49, 50].

In summary, even though a clear link between dynamics and intermittency has been pointed out, altering the dynamics does not change strongly the acceleration distribution. Further work remains to be done to analyze the interplay between dynamics and statistical properties. Note that following the experimental advance in Lagrangian tracking, this field of research is very active and for instance, some progress has been made recently by introducing a Lagrangian model for the evolution of the velocity gradient tensor which allows Chevillard & Meneveau to reproduce many features of the experimental velocity field [10].

1.5 Particle dynamics and scalar mixing

The issues of the dispersion of a passive scalar and that of fluid particles are intimately related as the scalar is carried by the fluid particles. For example, the average concentration of the scalar at a given position and a given time t is naturally related to the sources of scalar at times prior to t and to the

transition probability of a fluid particle to go from the source to the measurement position. This can be expressed formally as [56]:

$$\langle \theta(\mathbf{x}, t) \rangle = \int_{s \leq t} \int_V p_1(\mathbf{x}, t | \mathbf{y}, s) S(\mathbf{y}, s) d\mathbf{y} ds \quad (8)$$

where $S(\mathbf{y}, t)$ is the source strength and $p_1(\mathbf{x}, t | \mathbf{y}, s)$ is the probability for a fluid particle to go from (\mathbf{y}, s) to (\mathbf{x}, t) . This expression neglects the diffusivity of the scalar in the limit of high Reynolds and Péclet numbers and thus is not valid near the source [56]. For two-point and two-time correlations, similar expressions can be written which involve transition probabilities of the positions of two particles.

I want to discuss here a specific case of scalar transport: the case of a localized source. This is a typical situation for anthropic pollution for instance. For experimental simplicity, I investigate the case of a line source of scalar in a wind tunnel (i.e. in homogeneous and isotropic turbulence) in the same spirit of experiments by Warhaft [63] or Stapountzis *et al.* [57]. In the reference frame moving with the mean velocity of the fluid, this problem is equivalent to an impulse planar source of scalar at initial time [1]. The scalar is then dispersed by a decaying turbulent flow. The velocity component variance is decaying as a power law $\sigma_v^2(t) = \sigma_v^2(t_0)(1 + t/t_0)^{-m}$ where t_0 is the time of flight from the grid to the source. t is related to the downstream distance x by the Taylor hypothesis $t = x/U$ with U the average streamwise velocity. In moving reference frame, the properties of the flow such as σ and ϵ are evolving with time. I introduced above a stochastic modeling of the particle dispersion with a Langevin equation (3) for stationary homogeneous isotropic turbulence. This model is modified to take into account the energy decay [1]:

$$dv = - \left(\frac{1}{3} + \frac{C_0}{2} \right) \frac{\epsilon}{\sigma_v^2} v dt + \sqrt{C_0 \epsilon} dW \quad (9)$$

The transport of the scalar can then be modeled using a second stochastic equation

$$dy = v dt + \sqrt{2\kappa} dW_1 \quad (10)$$

where y is the position of the scalar particle, κ is the scalar diffusivity and dW_1 is another Wiener process, independent of the first one, introduced to take into account the diffusivity of the scalar. This model of dispersion, equations (9) and (10), has been solved by Anand & Pope [1] to obtain the mean spanwise concentration profiles. In that case, the profiles are gaussian and centered on the source position. The width σ_y of the profile is increasing with time (or equivalently with the downstream distance due to the Taylor hypothesis) following:

$$\sigma_y^2(t) = \sigma_0^2 + 2\kappa t + 2\sigma_v^2(t_0)t_0^2 \left(\frac{(1 + t/t_0)^{r-s}}{r(r-s)} + \frac{(1 + t/t_0)^{-s}}{rs} - \frac{1}{s(r-s)} \right), \quad (11)$$

with

$$r = \frac{m}{2} \left(\frac{3C_0}{2} - 1 \right) + 1, \quad (12)$$

$$s = \frac{m}{2} \left(\frac{3C_0}{2} + 1 \right) - 1. \quad (13)$$

At very small times the increase of σ_y^2 is linear and due to molecular diffusion. It is followed by a ballistic increase $\sigma_y \propto t$ due to turbulent transport for times smaller than the Lagrangian correlation time. Ultimately a subdiffusive behaviour is observed $\sigma_y^2 \propto t^{2-m}$ due to the decay of energy (m is usually observed between 1 and 2). It would be diffusive for stationary turbulence.

To check this prediction, we use the wind tunnel described in [35] that was built by myself for turbulence experimental courses of the Département de Physique at ENS (this data is unpublished to this day). Romain Bassez (Master student) did the preliminary experiments leading to the following results. Turbulence is generated by an active grid (with 20 rods and not 10 as in [35]). This device is quite efficient at generating highly turbulent flows in wind tunnels (even that of a moderate size). A self similar decay regime is observed with $m = 1.42$ and a Reynolds number $R_\lambda = 240$ at the scalar source with a mean velocity equal to 5.5 m.s^{-1} . Note that this Reynolds number is significantly higher than

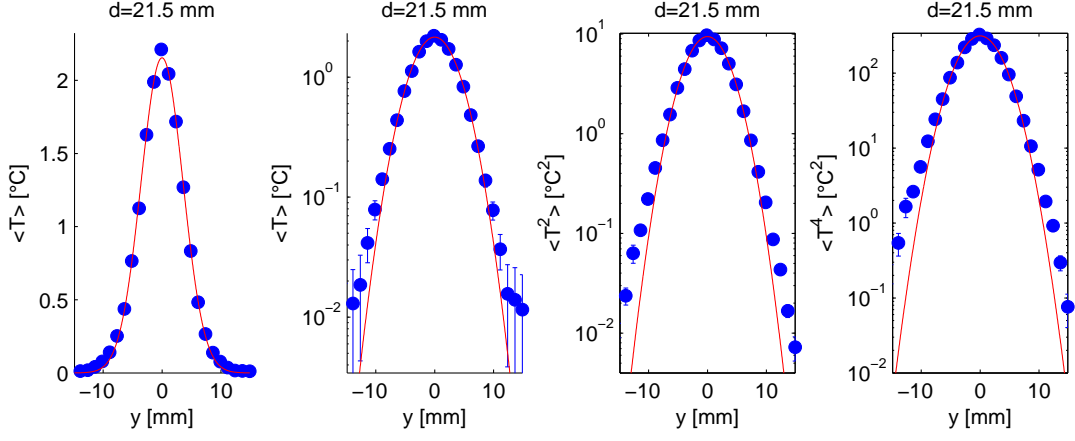


Figure 10: Spanwise profiles of the first (linear and semilog scale), second and fourth moments of temperature at 21.5 mm downstream the heat source. Solid lines are gaussian fits.

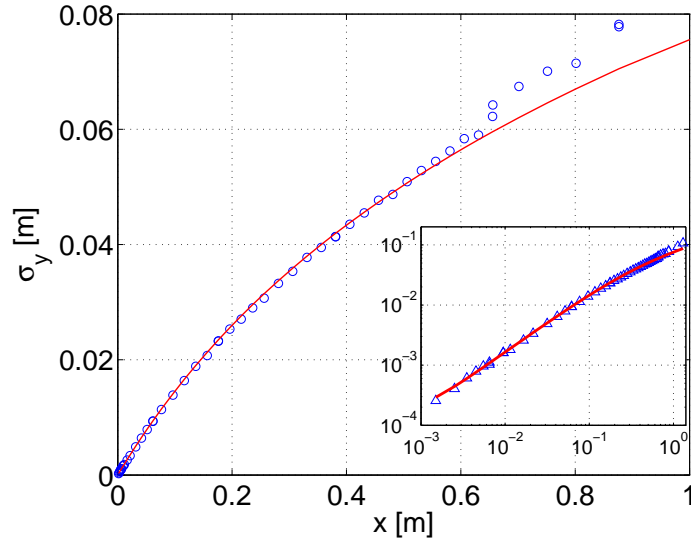


Figure 11: Width of the average temperature profiles as a function of the distance downstream the source. Circles are measurements, the solid line is the model prediction (11) with $C_0 = 2.7$. Inset: same in loglog scale.

previously available data such as [63, 57]. A linear source of temperature is made of a resistive wire whose temperature can be tuned by the intensity of the electrical current flowing in it. Temperature fluctuations are recorded downstream the source by a cold wire, $1.5 \mu\text{m}$ in diameter.

An example of a spanwise temperature profile is shown in figure 10. The average temperature profile is seen to be indeed very close to a gaussian profile as previously reported [63, 57]. Higher moments profiles are also very close to gaussian profile. Nevertheless a close look at the decay of the average temperature on the tails of the gaussian profile shows that the experimental profile decays slower than Gaussian. The effect is weak on the average profile but more visible for higher moments. The evolution of the width of the average temperature profile is shown in figure 11. Again, the prediction of the model is very good with a single free parameter C_0 (the fitted value is $C_0 = 2.7$). When the downstream distance is larger than about 0.6 m, the scalar profiles reach the walls of the tunnel, altering the dispersion mechanism so that the agreement with the model is no longer as good. For the average temperature, the simple Anand & Pope model is very efficient at describing the data. For higher order moments, models for N particles dispersion are required to get equivalent predictions for N -th order moments...

One question that arises from the previous studies of Lagrangian particles is the role of intermittency in the scalar dispersion. It is well known that the scalar intermittency can arise even without velocity intermittency [21]. One dynamical feature that could have some impact on the spread of the scalar plume

is the trapping of fluid particles in intense vortices. Initial (large) concentrations of scalar could be spread far from the source and be only weakly diluted by the flow. The observation of the slower than gaussian decay of the spanwise profiles may be related to this phenomenon but could as well be due to some experimental artifact or to the necessity to find a more adequate model (even without intermittency). This deserves much more investigations and numerical simulations may be of great help in this task, for example by simulating gaussian velocity field without intermittency and looking for differences in the scalar dispersion.

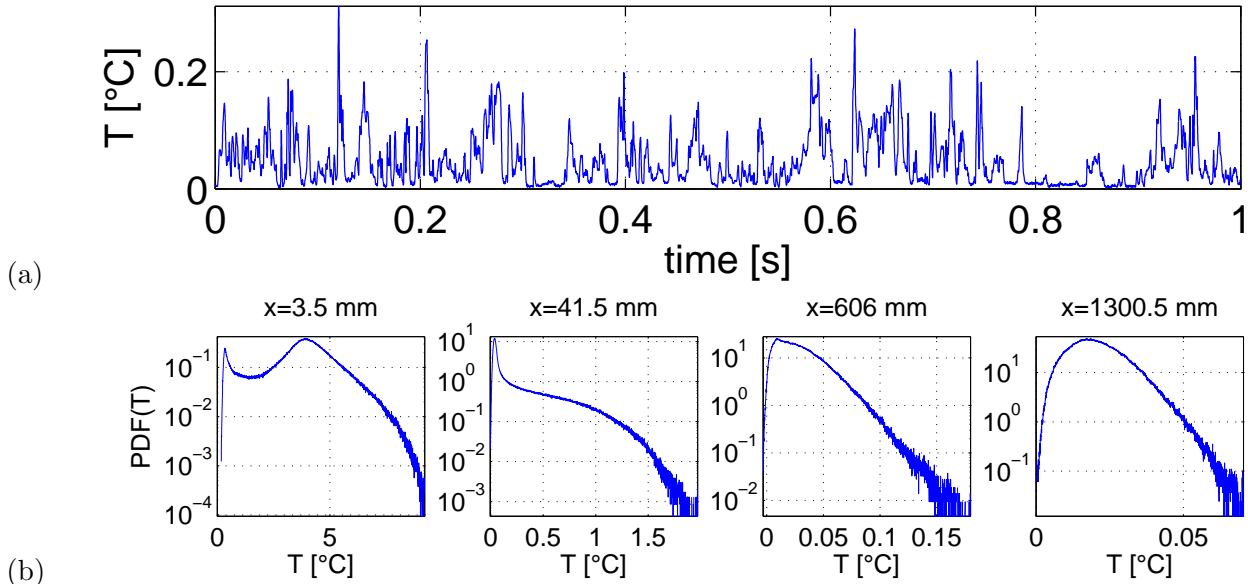


Figure 12: (a) Time series of the temperature measured at 41.5 cm downstream the heat source. Zero corresponds to the ambient average temperature. (b) Examples of distributions of temperature fluctuations at various distances downstream the heat source.

It should be noted however that the formal link between scalar moments and particle dispersion may be of little use for predictions in practical situations. A time series of temperature is shown in figure 12(a). The signal is very intermittent with periods of low temperature related to the ambient incoming temperature and strong bursts of hot fluid. Part of this variability comes from the simple meandering of the thermal wake in the vicinity of the source. Another part comes from the mixing process. Figure 12(b) shows some examples of distribution of temperature fluctuations. Very close to the source, a bimodal distribution is seen, due mostly to the meandering of the wake. Further downstream only one maximum is retained that corresponds to cold ambient fluid. A wide stretched exponential tail is visible all the way downstream to the exit of the wind tunnel. The existence of such a wide tail of the distribution of scalar could be of importance in practical situations (release of hazardous chemicals for instance). Understanding this process and its link with the properties of the flow is a very ambitious task. Nevertheless if one wishes to model such a mixing process in realistic situations (for instance a localized release of pollutant in the atmosphere) a model based on the estimation of successive moments may not be very efficient as high order moments are required to describe the observed distributions.

An alternative may be to describe the observed PDFs in terms of model distributions. Figure 13 displays the evolution of the flatness of the temperature fluctuations versus the skewness. A relationship between flatness and skewness can be observed with two branches. The low branch corresponds to positions of the measurement close to the source: points with $F \approx 2$ and S small are the closest to the source and one progresses to the other end of the branch (high S and F) when moving downstream or when moving away from the centerline. The second branch corresponds to the furthest downstream positions when the scalar is more mixed. The points with $F \approx 3$ are the points on the centerline near the exit of the tunnel. Two classes of distributions are therefore present, one corresponding to badly mixed scalar including the bimodal distributions and the other branch for well (better?) mixed scalar for the statistics is expected to become gaussian asymptotically. At high S both branches are superimposed and

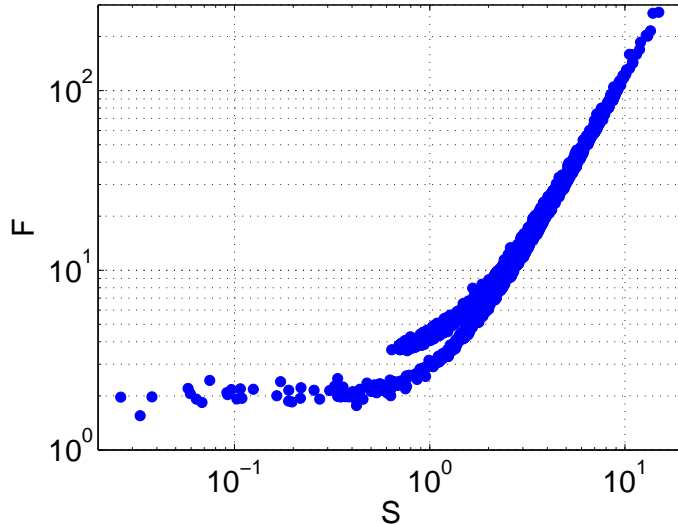


Figure 13: Cumulative plot of the flatness vs skewness of the temperature fluctuations. Accumulation of many downstream positions and three different Reynolds numbers $R_\lambda = 240, 190$ and 140 (at the source location). Only data for which the uncertainty on both quantities is less than 25% have been retained.

F behaves quadratically with S . The lower branch has been reported in the literature and may be consistent with a family of bimodal distributions (see [30] for recent work and references therein). A criteria for the transition from one branch to the other still has to be specified. The origin of these families of distribution still have to be precised on fundamental grounds. The analysis of the scalar dispersion data is still underway.

The new Lagrangian tracking techniques in the last decade have provided new experimental data and triggered a renewed dynamics in modeling and numerical simulations. Much progress has been done in the understanding of the dynamical origin of intermittency but the quantitative link between dynamical models and statistical dispersion is still underway. The link between models of scalar dispersion and the properties of the dispersion of Lagrangian particles is formally expressed. Nevertheless practical implementation in numerical schemes is still a challenge. Confrontations between experimental observations for two particles and higher order scalar dispersion models still has to be made to my knowledge although many stochastic models exists.

I am personally interested in future experimental study of Lagrangian statistics in a boundary layer which is a benchmark of non homogeneous turbulence. This has many motivations from environmental studies in particular. One important application is the dispersion in the atmospheric boundary layer which is directly related to human activity. Very few experimental data exists so far in spite of the wide interest of the problem.

2 Magnetohydrodynamics and dynamo

Magnetohydrodynamics concerns the motion of conducting fluids coupled to the evolution of the magnetic field. For high magnetic Reynolds number Rm (Reynolds number based on the Joule dissipation rather than on the viscosity), depending on the intensity of the magnetic field (quantified in non dimensional units by the interaction parameter N), the magnetic field can be passively transported ($N \ll 1$) or can play a dynamical role and act on the fluid motion ($N \gg 1$). In the first case, the magnetic field behaves as a passive vector which main difference compared to the scalar case is the possibility of amplification by an adequate geometrical configuration of the flow [62]. In some cases, this amplification can lead to a sustained generation of a magnetic field from initial magnetic traces: the dynamo effect. Dynamo is an instability which onset is determined by a balance between amplification and dissipation of electrical cur-

rents by Joule effect. This effect is generally accepted as the origin of the magnetic fields of astrophysical objects such as planets, stars and galaxies.

Even if the principle of magnetic field generation by a clever motion and arrangement of solid electrical conductors was implemented at the end of the 19th century, more than one century was needed to see an experimental fluid dynamo in Riga and Karlsruhe [23, 59]. In these two cases, the flow was constrained to resemble analytical models. In both cases, the dynamo onset and the generated magnetic fields are in close agreements with predictions based on the average flow. Turbulent fluctuations do not have a strong influence on the dynamo characteristics. One open question is how a fully turbulent flow with strong fluctuations at all scales can sustain a dynamo process, and in particular how it does affect the instability threshold and the magnetic field geometry as compared to predictions based on the average flow only. To address this question, the VKS experiment was built in collaboration between CEA, ENS de Lyon and ENS de Paris. The core of the flow is a Von Kármán flow between two coaxial disks. The VKS experiment was able to sustain a dynamo for the first time in 2006 [32]. A large variety of dynamical regimes of the magnetic field was observed (reversals, oscillations, bursts...).

In addition to this technically demanding experiment, several water or gallium experiments were developed in the three institutions of the collaboration. In Paris, we developed a gallium experiment during the PhD of Michaël Berhanu [5] (codirected by myself and S. Fauve). With B. Gallet (also PhD student in our group), we studied in particular the influence of a large magnetic field on a turbulent flow of gallium to have some insight on the last part of the development of a dynamo magnetic field. In a typical supercritical dynamo, the magnetic field first grows exponentially due to linear amplification. Then it reaches large enough values so that it can react on the fluid motion through the Lorentz (Laplace) force. We studied in a gallium flow (at a much lower magnetic Reynolds number than in the VKS experiment) the damping of the turbulent fluctuations as will be presented below.

In this section, I will very briefly recall the theoretical background of MHD, then present the results of the influence of a large magnetic field on a gallium turbulent flow. Finally, I will describe the most prominent features of the VKS dynamo.

2.1 Fundamental equations of MHD

The basic equations of MHD are the Navier-Stokes equation for the fluid flow and the induction equation of the evolution of the magnetic field. The former can be written as:

$$\frac{\partial \mathbf{v}}{\partial t} + (\mathbf{v} \cdot \nabla) \mathbf{v} = -\frac{1}{\rho} \nabla p + \nu \Delta \mathbf{v} + \frac{1}{\rho} \mathbf{j} \times \mathbf{B} \quad (14)$$

where ρ is the fluid density, p the pressure, \mathbf{j} the current density. We consider incompressible fluids so that $\nabla \cdot \mathbf{v} = 0$. The last term in (14) is the Lorentz force and is the way the magnetic field \mathbf{B} can act on the flow dynamics. The induction equation is written, for non relativistic liquid metals:

$$\frac{\partial \mathbf{B}}{\partial t} = \nabla \times (\mathbf{v} \times \mathbf{B}) + \frac{1}{\mu_0 \sigma} \Delta \mathbf{B} \quad (15)$$

where μ_0 is the vacuum permeability and σ is the electrical conductivity. $\eta = 1/\mu_0 \sigma$ is the Joule diffusivity of the magnetic field.

Three independent nondimensional parameters can be defined: the usual Reynolds number UL/ν , the magnetic Reynolds number UL/η and the interaction parameter $N = \sigma B^2 L / (\rho U)$. The interaction parameter N measures the intensity of the Lorentz force compared to the inertial forces. The two Reynolds numbers are related by $Re = (\eta/\nu) Rm = Rm/Pm$. Pm is less than 10^{-5} for sodium and gallium so that Re must be large in order to have Rm at least of order one. This implies that the flow will be highly turbulent. One drawback of this natural constraint is that the experiments will consume a large mechanical power to sustain the flow. This is a major financial and mechanical constraint for dynamo experiments.

2.2 Influence of a strong magnetic field on a turbulent gallium flow

2.2.1 The D24 gallium experiment

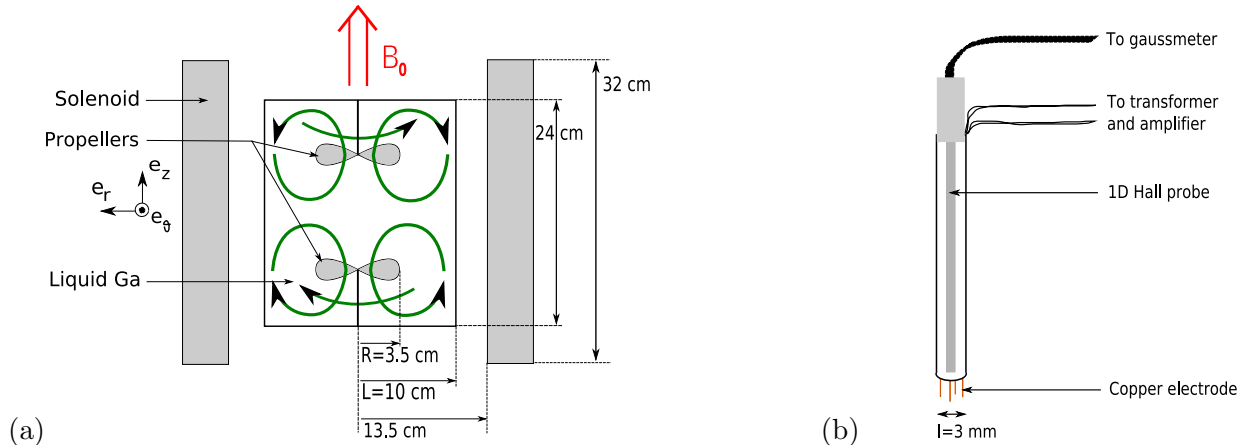


Figure 14: (a) Sketch of the gallium experiment. (b) sketch of the potential probes with two pairs of electrodes. Figures from [24].

During his PhD, Michaël Berhanu developed a Gallium experiment at ENS [5]. The setup was relatively versatile and he characterized the hydrodynamics and the low magnetic field induction properties of a large family of flows. The geometry chosen to study the influence of large magnetic fields is sketched in figure 14(a). The flow is entrained by two counter-rotating propellers with a global geometry similar to a von Kármán flow. The whole experiment is placed inside a solenoid which can generate a magnetic field \mathbf{B}_0 up to 1600 G. The velocity is of order $2\pi R f_{rot}$ (where f_{rot} is the rotation frequency of the propellers) so that the interaction parameter can be defined as $N = \sigma L B_0^2 / (2\pi \rho R f_{rot})$. It can reach values up to 2.5 [24]. The Magnetic Reynolds number is close to unity and the kinetic Reynolds number is of the order 10^6 , so that the flow is fully turbulent even at low rotation rates. The main advantage of our flow compared to preexisting work, lies in the absence of bifurcation of the flow geometry when the magnetic field is increased (see [24] and references therein).

We used potential probes (figure 14(b)) that measure the electrical potential induced by the motion of the fluid onto a pair of electrodes separated by a close gap [5, 6, 24] (about 3 mm in our case). The link between the measured potential and the velocity is not straightforward. The basic equation is

$$\Delta\phi = \omega \cdot \mathbf{B}_0 \quad (16)$$

when the induction is negligible compared to the applied field (which is the case here). ϕ is the electrical potential and ω is the vorticity. We measure the potential difference $\delta\phi$ across the electrodes. For length scales larger than the electrode separation l , $\delta\phi$ is proportional to the gradient of the potential and the scaling of its spectra is the same as that of the velocity fluctuations ($\propto k^{-5/3}$). For length scales much shorter than l , $\delta\phi$ is the difference of two independent measurements so that the spectrum of $\delta\phi$ is expected to be $\propto k^{-11/3}$. The link between potential and velocity is not direct but the spectral characteristics of the potential difference should reflect that of the velocity with some complex filtering contributions.

2.2.2 Pertinence of the interaction parameter

The standard deviation of the electrical potential and the induced magnetic field are plotted in figure 15 (a,b) as a function of the rotation rate of the propeller and the imposed magnetic field. For high speed and low B the *rms* values are evolving linearly with the magnetic field but a departure from linearity is observed for increasing B . The departure is more pronounced for low speeds. The behavior of the induced magnetic field is the same. When the Rm is low and the induction negligible, the induction

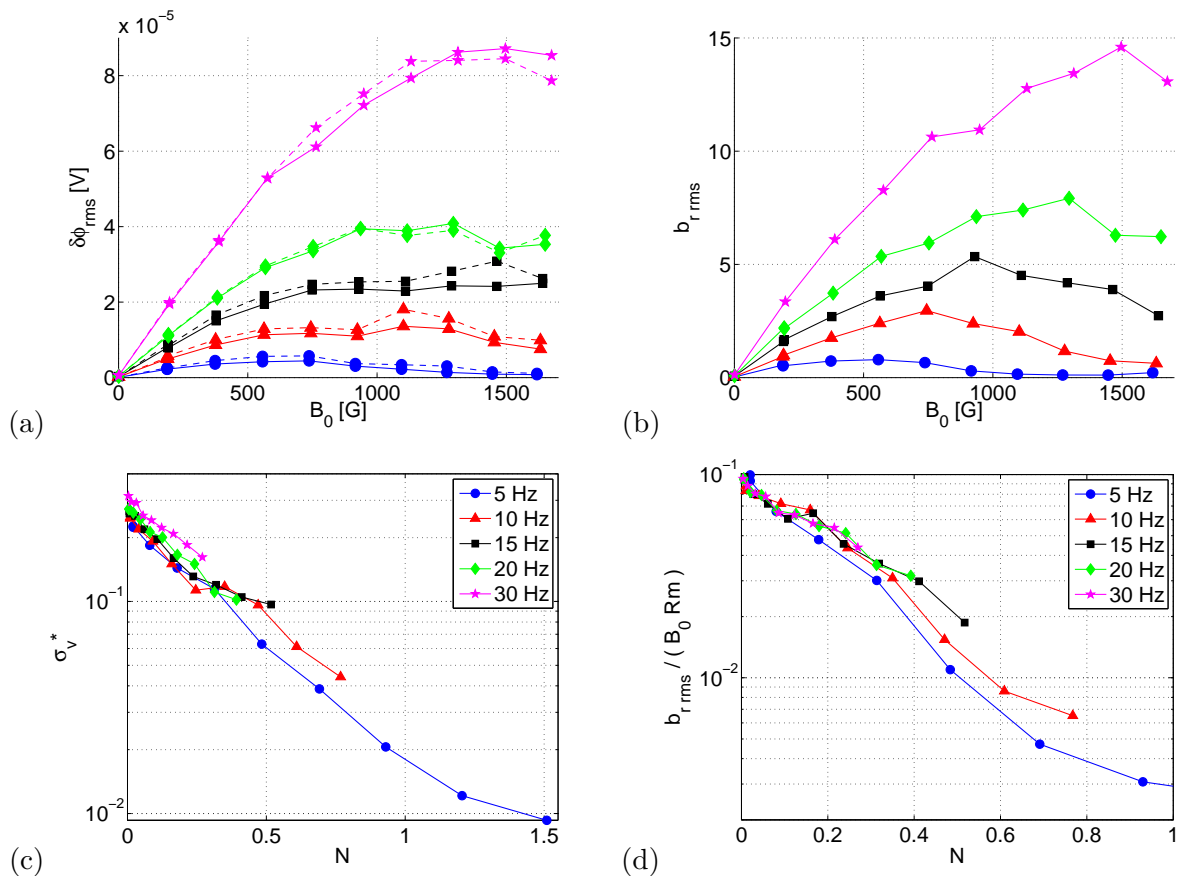


Figure 15: Evolution of the *rms* potential (a) or induced magnetic field (b) as a function of the applied magnetic field for various rotation rates. Decay of the dimensionless potential (c) and magnetic field (d) fluctuations as a function of the interaction parameter for various rotation velocities. Figures from [24].

equation (15) reduces to

$$\mathbf{B}_0 \cdot \nabla \mathbf{v} + \eta \Delta \mathbf{b} = 0, \quad (17)$$

where $\mathbf{b} = \mathbf{B} - \mathbf{B}_0$ is the induced magnetic field. It means that the induced magnetic field is simply a picture of the gradients of velocity along the applied magnetic field whereas the electrical potential is a picture of the velocity gradients perpendicular to \mathbf{B}_0 .

The potential difference standard deviation can be non dimensionalized as $\sigma_v^* = \delta\phi_{rms}/(BIRF_{rot})$ and the magnetic field fluctuations as $b_{rms}/(B_0 R m)$. Both quantities are displayed versus the interaction parameter N in figure 15(c,d). The various curves at different velocity are fairly superimposed. In non dimensional units, both potential and induced magnetic field show a decay of the fluctuations intensity which seems close to an exponential decay. The decay can reach over one order of magnitude for the highest value of N . We conclude from these observations that the interaction parameter is the relevant control parameter of this phenomenon. When increasing N , the velocity fluctuations are strongly damped up to one order of magnitude when N reaches unity.

A dynamical picture of this kind of magnetic braking is obtained from the Fourier spectra of the dimensionless potential differences shown in figure 16. For a given value of N the spectra corresponding to different rotation rates f_{rot} are fairly superimposed. When N increases, two features can be observed. First, at low frequencies, the spectra are damped in an equal way at all frequencies (i.e. without changing their shape). Second, at the highest resolved frequencies, the damping is stronger resulting in a steepening of the decay of the spectra with increasing N . All scales are influenced by the magnetic field contrary to what was first expected by Bachelor for instance (see [6, 24] for more details).

These results can be related to the issue of the saturation of the dynamo. If the dynamo field was generated by turbulent fluctuations of the velocity (e.g. $\alpha\omega$ dynamo as the VKS dynamo could be) then the back-reaction of the growing dynamo magnetic field on the flow would alter its amplification properties

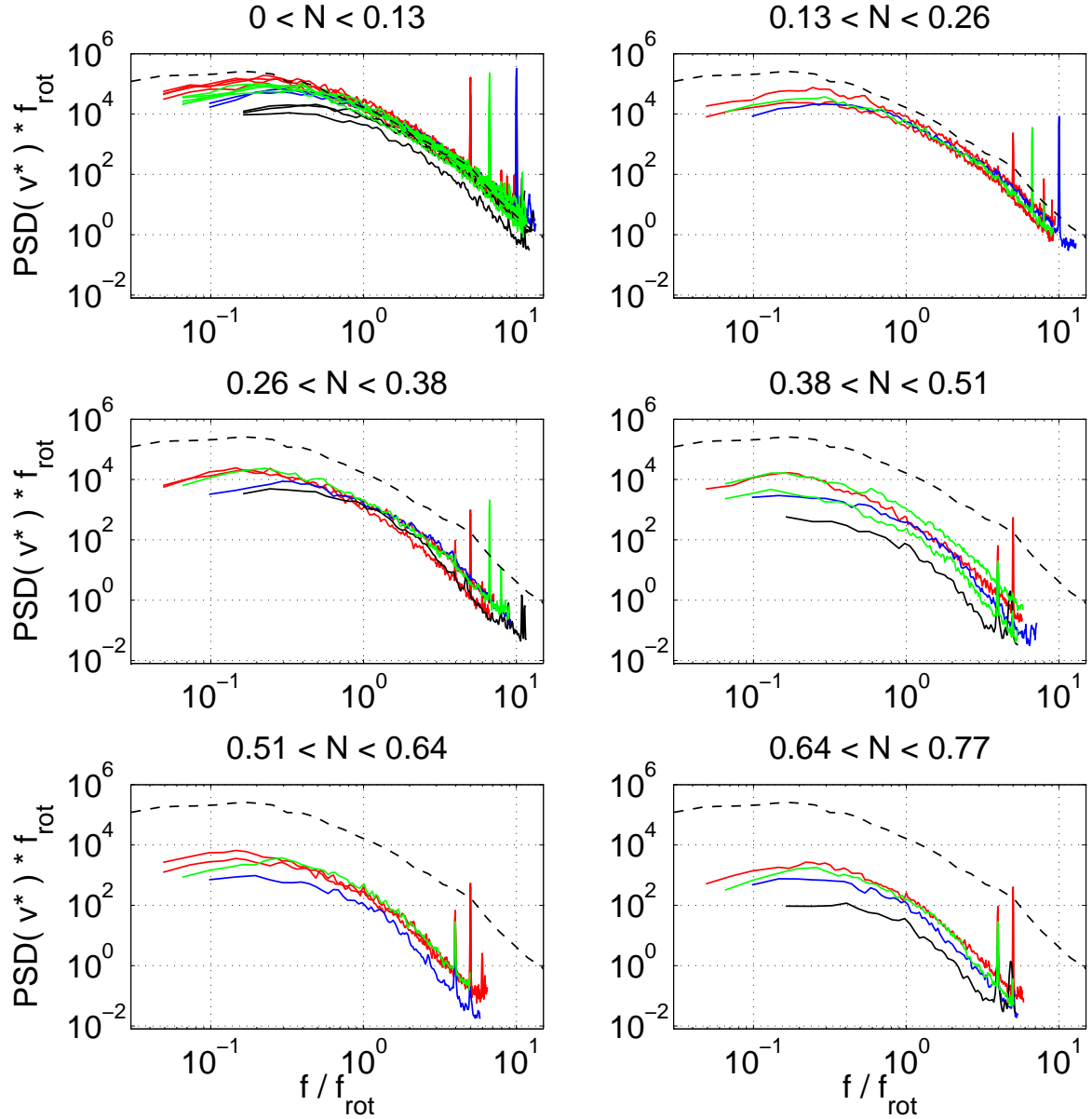


Figure 16: Time Fourier spectra of the potential difference (in non dimensional units). Colors corresponds to various velocities (black: 3Hz, blue: 5Hz, green: 7.5Hz and red: 10Hz). The spectra are gathered in groups of similar values of N . The dashed line is the spectra corresponding to the smallest value of N in the dataset. Figures from [24].

and possibly lead to a saturation. In the gallium flow, the damping of the turbulent fluctuations is seen to be $\sigma_v^* \propto \exp(-cB^2/f_{rot})$ (with some geometrical constant c) which is very strong. It could be very efficient at stopping the growth of the magnetic field. Based on our observations in the gallium flow, an order of magnitude of the expected saturated magnetic field in the VKS case is consistent with the recorded values (see [24]).

2.3 The VKS experiment: turbulent dynamical dynamos

The VKS experiment is the result of the collaboration of about 20 persons from three institutions (ENS de Lyon, ENS de Paris, CEA Saclay). This collaborative effort around the dynamo in a Von Kármán flow

started at the end of the 90's and succeeded in obtaining a dynamo in 2006. I joined the collaboration in 2004 to participate to the last bits of construction of the second version of the experiment called VKS2. I did not take part in the first version (whose runs occurred during my PhD on Lagrangian particles) nor in the technical definition of VKS2.

The experiment is located in CEA Cadarache in the south of France where the expertise on sodium handling and safety existed before VKS.

2.3.1 Experimental setup of VKS

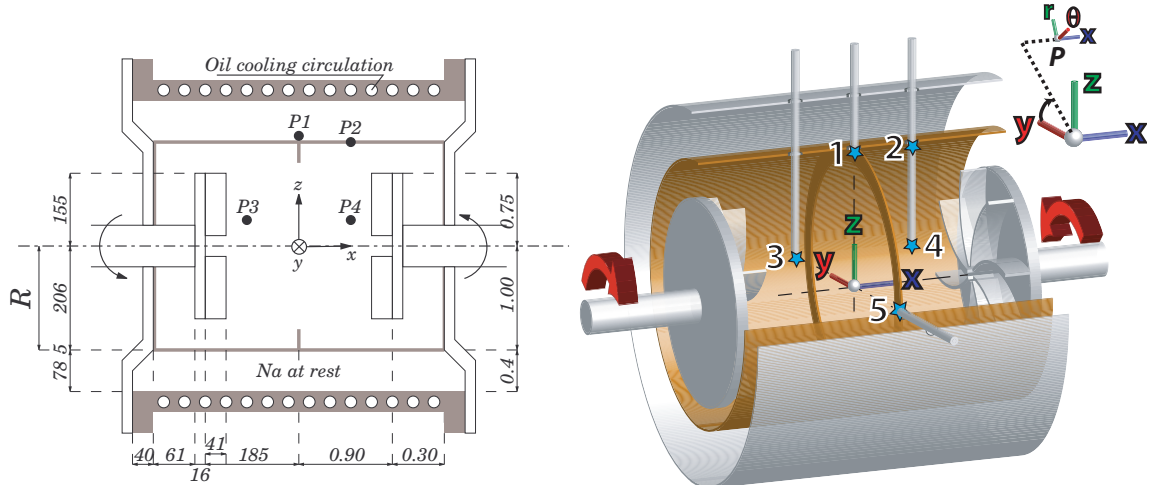


Figure 17: Experimental setup. Note the curved impellers, the inner copper cylinder which separates the flow volume from the blanket of surrounding sodium and the thin annulus in the mid plane. Also shown are the holes through which the 3D Hall probes are inserted into the copper vessel for magnetic measurements. When referring to the coordinates of magnetic field vector \mathbf{B} measured in the experiment at these different points, we will use either the Cartesian projection (B_x, B_y, B_z) on the frame (x, y, z) or the cylindrical projection (B_r, B_θ, B_x) on the frame (r, θ, x) ($B_\theta = -B_y$ and $B_r = B_z$ for measurements at points $P1, P2$ and $P3$). Unless otherwise noted, we will use in figures the following color code for the magnetic field components: axial (x) in blue, azimuthal (y) in red and radial (z) in green. Figures from [31].

Sketches of the experimental vessel of the VKS experiment with all appendices are shown in figure 17 (see [31] for more details on the experiment). The exterior vessel is a copper cylinder containing 150 liters of sodium. Many appendices have been added to this vessel after an optimization procedure based on kinematic simulations based on experimental water flows [52]. Its inner volume can be split into two compartments (roughly equal in volume) by the addition of a copper cylinder. This is motivated by the benefits of an outer layer of conducting material at rest as a radial boundary. The inner cylindrical volume is the core von Kármán flow driven with two impellers fitted with curved blades. Tuning the curvature of the propeller blades changes the ratio of the amplitude of the poloidal over toroidal parts of the flow. The material of the propeller has been changed several times in the various runs of VKS2 (copper, stainless steel, pure iron, stainless steel with a layer of vacuum behind). Finally a small copper annulus can be added in the mid plane to stabilize the shear layer that is at the boundary of the two recirculation cells generated by the motion of the impellers in counter-rotation [52]. The first dynamo configuration was obtained with the full set of appendices and iron propellers. Then dynamos were also obtained either without the annulus or without the cylindrical shell. Dynamos were also obtained with one iron disk and one stainless steel disk.

This cylindrical vessel is included in complex sodium and argon pipe recirculation loops for controlling the filling and safety of the experiment. Each impeller is driven by a pair of 75 kW motors controlled at constant rotation frequency (300 kW total mechanical power). Finally the temperature of the experiment is regulated by an oil cooling recirculation loop.

Measurements are relatively few in the VKS experiment. This is due to safety reasons that make

the inclusion of probes inside the experiment quite difficult and from the fact that the experimental configuration is in constant evolution in order to find, first, a dynamo configuration, and second, the dynamo configuration that would make multiple probes inclusion easier. Measurements are provided by a 3-axes Hall gaussmeter or by a specifically designed multiple probe array made of 10 three axes Hall probes on a radial line. The choice and position of the probes vary a lot from one configuration to another. The instantaneous power injection can be measured also through the industrial controllers of the motors. The temperature is monitored during the runs and can be slightly varied from about 110 to 160 Celsius degrees (sodium melts at 98 degrees). The lowest temperature leads to the highest magnetic Reynolds numbers due to the highest conductivity. Magnetic Reynolds numbers based on impeller velocity and inner cylinder radius can be varied up to about 50. The expected range of values for the critical Rm was up to 100 roughly from the kinematic simulations [52].

The rotation rate of the two propellers can be chosen independently. We refer to symmetric driving when the rotation rate is the same for both propellers (the propellers are then counter rotating at the same speed). Asymmetric forcing refers to different rotation rates of the propellers (but always in contra rotation due to technical reasons).

2.3.2 Dynamo with symmetric driving

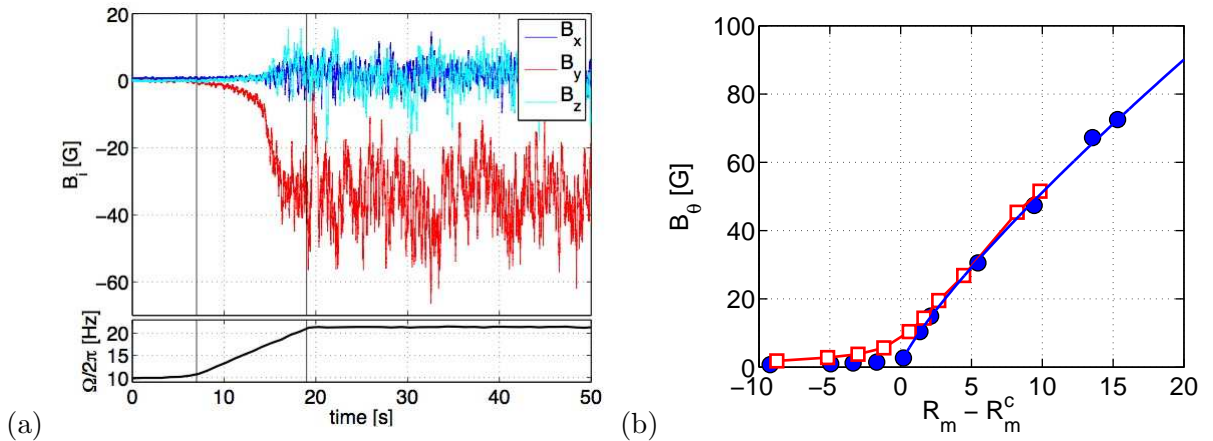


Figure 18: (a) Generation of the dynamo when accelerating the propellers in a symmetric configuration for a probe in position P1 of figure 17. (b) Azimuthal field versus magnetic Reynolds number. Blue: initially nonmagnetized iron impellers, red: magnetized impellers. Figures from [31].

An example of times series of a growing dynamo is shown in figure 18(a) (full set of appendices and iron impellers). The rotation speed of the impellers is increased to overcome the threshold. A strong azimuthal field is generated at the measurement point with a clearly defined non-zero average value and a fluctuating part (hence this dynamo is called “stationary dynamo”). The evolution of the average azimuthal field is shown in figure 18(b). This evolution is typical of a supercritical bifurcation with the critical magnetic Reynolds number $Rm^c \approx 32$ [32, 31]. The scaling exponent of the magnetic field amplitude over threshold is not $1/2$ as expected in classical bifurcations but takes larger values. It is not very clearly defined and deserves much more investigations to make any conclusion on possible non classical exponents.

Hints of the geometry of the dynamo mode can be inferred from multiple probe measurements as shown in figure 19(a). On the axis of the cylinder the axial component dominates. It decays when going off axis and the azimuthal field grows and finally goes to zero on the wall of the outer container. A sketch of the geometry is shown in figure 19(b) by extrapolation from various multiprobe measurements. To the best of our knowledge, the average field seems roughly symmetrical by rotation around the axis of the experiment with a strong dipolar component close to the axis and a strong azimuthal component constrained inside the vessel.

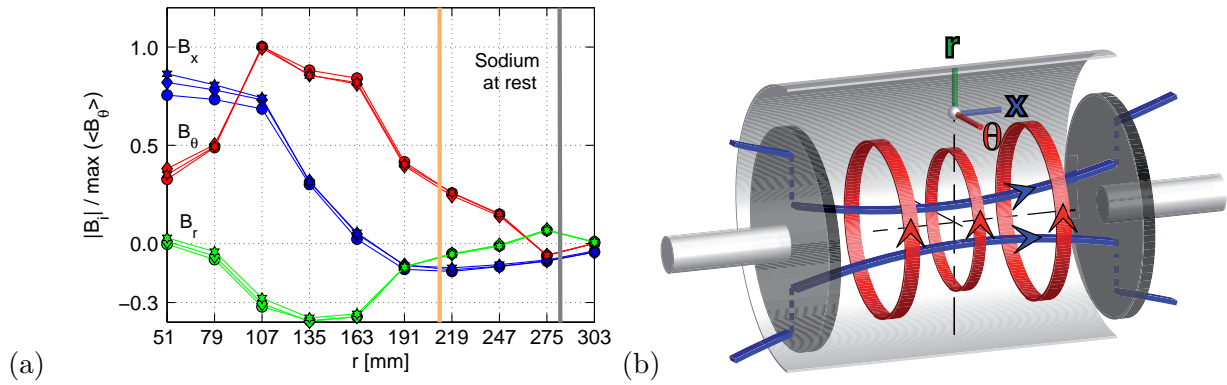


Figure 19: (a) Radial profile of the magnetic field for a probe in position P3 of figure 17. Symmetric driving of the motors. (b) Sketch of the inferred geometry of the dynamo field. Figures from [31].

2.3.3 Dynamos with non symmetric driving

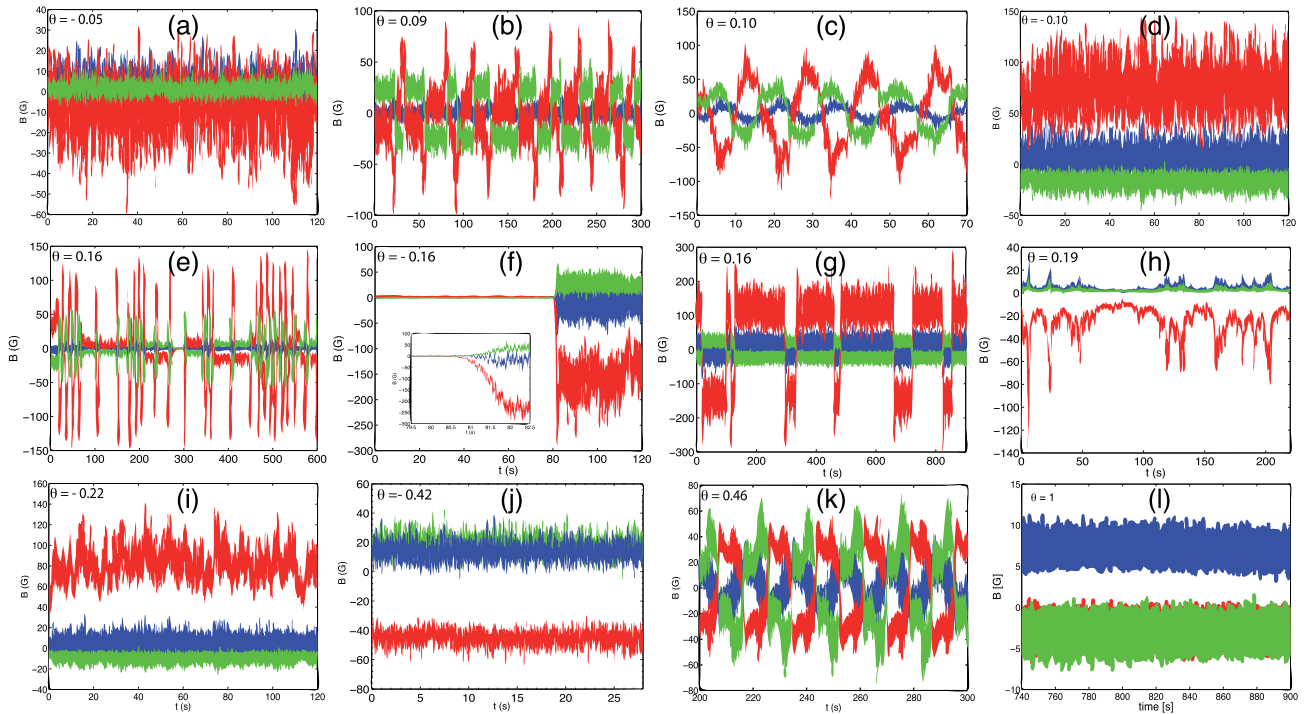


Figure 20: Examples of dynamos for various values of $\theta = \frac{Rm_1 - Rm_2}{Rm_1 + Rm_2}$. Color code for the magnetic field components: axial (x) in blue, azimuthal (y) in red and radial (z) in green. Setup with the full set of appendices. Figure from [31].

In the case of different rotation rates of the two impellers, two magnetic Reynolds numbers Rm_1 and Rm_2 are defined based on the velocity of each impeller. Another convenient parameter is $\theta = \frac{Rm_1 - Rm_2}{Rm_1 + Rm_2}$. When exploring the parameter space (Rm_1, Rm_2) a variety of dynamo regimes were discovered [7, 5, 3, 31]. Several stationary dynamos with different amplitude and fluctuation rates are separated by regions of dynamical dynamos, i.e. dynamos with large and slow fluctuations. Some classification was performed in the case of the full set of appendices [31] or without the annulus [5]. In the former case, four stationary dynamos were observed (fig. 20(a), (d),(i,j),(l)). For the dynamical dynamos, one can observe a limit cycle (fig. 20(b,c)), reversals (fig. 20(g)), bursts (fig. 20(e,h)), oscillations (fig. 20(k)). It was also possible to observe extinctions i.e. no dynamo (fig. 20(f)) very close to points where a dynamo was observed (and well above the threshold). For the configuration without annulus, details on the various observed dynamos can be found in [5]. Note that the equations of the dynamo problem are symmetric by the change $\mathbf{B} \rightarrow -\mathbf{B}$. Usually oscillating or reversing dynamos changed sign in a symmetric way. For most

stationary solutions, it was possible to observe both positive or negative polarities depending on the path followed in the parameter space to reach the stationary regime.

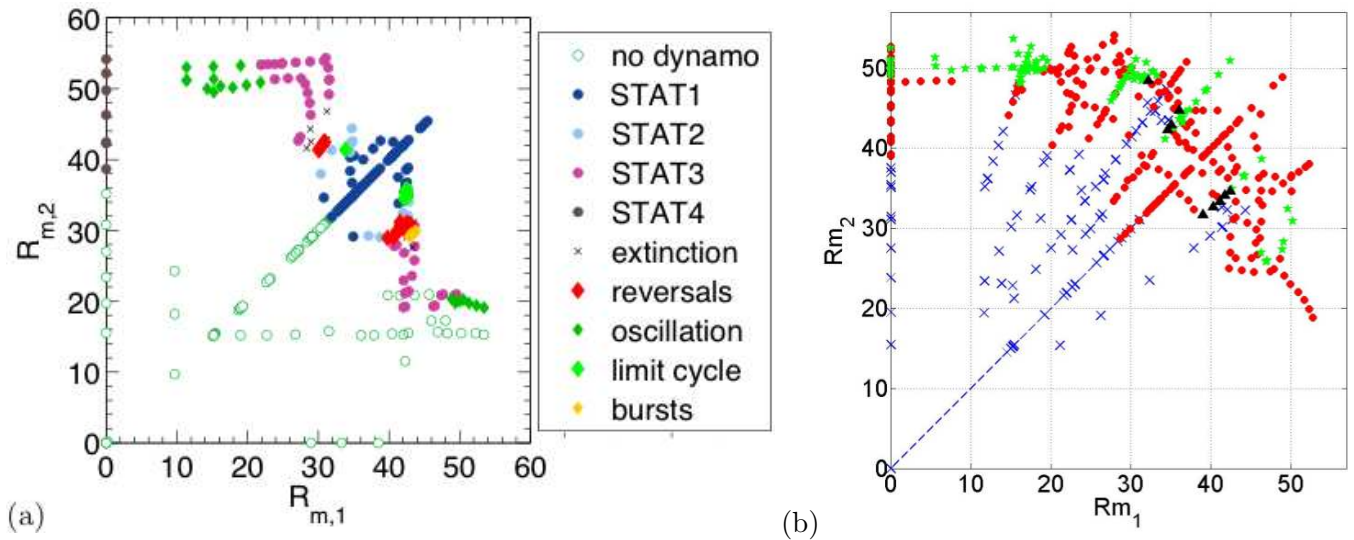


Figure 21: Parameter space: type of dynamo in the plane (Rm_1, Rm_2) . (a) Case with the full set of appendices. Figure from [31]. (b) same but without the annulus. x no dynamo (i.e. $< 10G$ at the center). Red dots: stationary dynamos. Green stars: reversing/oscillating dynamos. Black triangles: intermittent dynamos. Dashed line: $Rm_1 = Rm_2$. Figure from [5].

The parameter space is shown in figure 21 for the setup with full set of appendices and the case without annulus. Both parameter spaces are very similar and the dynamical dynamos share some strong similarity. Note that a dynamo was also observed with the cylindrical shell but without the annulus when counter rotating the impellers with negative frequencies. In that case, the threshold seems to be much higher. When no annulus is present and only one disk is turning bistability is present with a stationary and a reversing dynamo observed for the same set of parameters but with different paths in the parameter space. Without the inner cylinder, the variety of dynamos is much lower. Finally a dynamo was also observed with one iron impeller and the other one made of stainless steel.

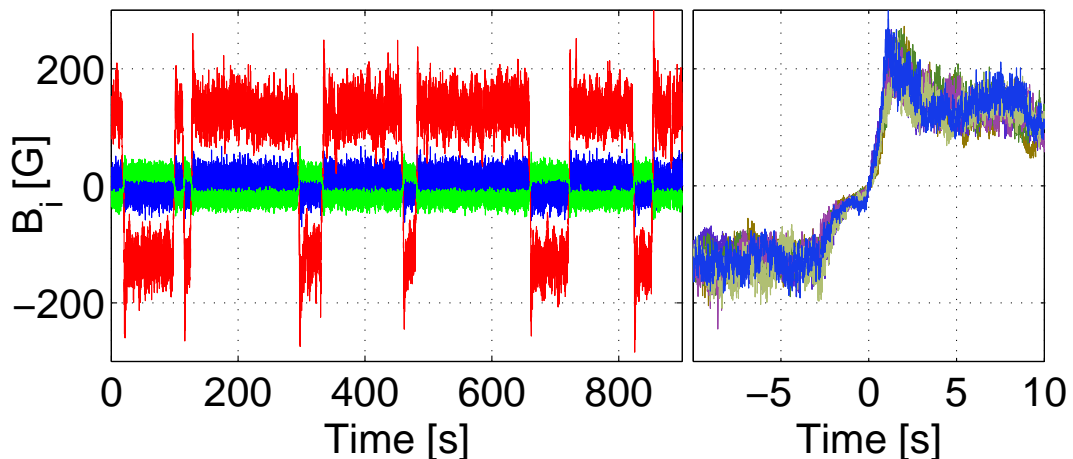


Figure 22: Reversals of the magnetic field at frequencies $F_1 = 16$ Hz and $F_2 = 22$ Hz ($\theta = 0.16$). (a) Time recording of the three magnetic field components at $P2$: axial (x) in blue, azimuthal (y) in red and radial (z) in green. (b) Superimposition of the azimuthal component for successive reversals from negative to positive polarity together with successive reversals from positive to negative polarity with the transformation $B \rightarrow -B$. Figure from [31].

The most striking kind of dynamo is the so-called reversal (figure 22) [6, 31]. The magnetic field displays almost constant phases of either sign separated by reversing phases. The reversing phases show

a very robust and repeatable structure: a slow decay (of duration close to the Joule dissipation time) followed by a sharp increase and an overshoot before reaching the stationary phase. The duration of the stationary phases is random with strong differences from one phase to another. All these features are reminiscent of the reversals of the Earth magnetic field and suggest a common physical mechanism even though our setup is quite different from the Earth geometry and flow.

2.3.4 A mechanism for the generation of the VKS dynamo

In the Riga and Karlsruhe dynamos [23, 59], the threshold and geometry of the dynamo field were in good agreement with kinematic simulations of calculations based on the average flow. Indeed, the flow was strongly constraint and the turbulence level was relatively low. For VKS in the symmetric forcing case, the average flow is symmetrical around the axis of the experiment and the magnetic field seems to share the same geometry. If the dynamo is generated only by the average flow, both flow and magnetic field can not share this cylindrical symmetry by Cowling's theorem. Assuming that the cylindrical geometry of the magnetic field is granted, this suggests that non symmetrical components of the flow must take part in the process generating the magnetic field. Kinematic simulations of the induction equation using the average flow of VKS (measured in water) have shown that the geometry of the expected dynamo is dipolar but the axis of the dipole lies in the mid-plane of the cylinder and not on its axis so that to be in agreement with Cowling's theorem [52].

The VKS flow being strongly turbulent, it is never axisymmetric and thus it is possible to sustain a cylindrically symmetric dynamo thanks to the fluctuations. We have suggested a mechanism for the generation of the VKS dipole [47]. It is very likely that 8 radial vortices exist in between the blades of the impellers. Due to the centrifugal pumping a radial flow coexists in the same region of the flow leading to some helicity. Helicity is known to be efficient in induction processes (by microscopic α effect or by macroscopic Parker effect) [29] and is expected here to generate a poloidal magnetic field from a toroidal one. Our mechanism involves non stationary large scale structures rather than small scale turbulence. Besides, dynamo generation is usually achieved by a two induction steps positive loop-back amplification. The second induction step is provided by a ω -effect due to the counter rotation of the impellers [8]. This suggests an $\alpha\omega$ dynamo for VKS. Laguerre *et al.* verified that a α effect localized near the impellers could generate an axial dipole. Nevertheless the requested level of the α parameter is very high [27]. Gissinger checked that macroscopic radial vortices can play the same role [26]. Again the intensity of the vortices has to be fairly high. Therefore this suggested mechanism is plausible but more work remains to be done to have a better understanding of the induction processes in VKS. In particular, simultaneous measurements of the magnetic field and the flow velocity could be implemented in the experiment to provide hints of the induction mechanisms.

2.3.5 Influence of the boundary conditions

Boundary conditions play an important role in VKS. For instance, when both impellers are made of stainless steel, no dynamo can be generated with the values of magnetic Reynolds number that are reached with our setup. Soft iron is required to observe the dynamo. Recent results of VKS show that when using only one iron disk a dynamo can still be seen. The role of the iron disks can be twofold. First, it can magnetically shield the core flow from the flow behind the impellers. Kinematic simulations show that this secondary flow always plays a negative role in the induction mechanism and can increase the threshold very significantly, possibly out of reach of our experiment [58]. Second, iron is a soft ferromagnetic material which means that it has a low remanence and a high magnetic permeability. The high permeability changes the boundary conditions of the magnetic field. This effect seems to be always positive in lowering the dynamo threshold [25]. It can be expected that an inner cylinder made of iron should also favor dynamo generation in VKS. This configuration is to be tested in the near future.

Another effect of the iron disks is to render the bifurcation imperfect as shown above in figure 18(b). When the disk is not magnetized (after an oscillating regime for instance), the bifurcation curve is the blue one and the dynamo can start with whichever polarity of the dipole. If the speed is decayed then the bifurcation curves turns into the red one with a smooth transition typical of imperfect bifurcation and

most likely due to the small remanence of the iron impellers. This contribution is rather weak and most likely restricted to the vicinity of the dynamo threshold. A simple phenomenological model described in [47] supports this scenario.

Other features of the vessel are intended to change the boundary conditions. The hydrodynamical role of the annulus is to stabilize the shear layer whose instability may alter the dynamo generation. The removal of the annulus does not change much of the threshold level but does change somewhat the ordering of stationary/dynamical dynamos. On the other hand, the removal of the inner cylinder changes more than just the boundary conditions as the geometry of the flow is also changed. Most dynamical regimes disappear when removing the inner cylinder. We tried also to rotate stainless steel impellers with a layer of gas behind to have insulating boundary conditions behind the disks. It was not possible to generate a dynamo as was also the case for simple stainless steel impellers.

The issue of the boundary conditions is a key to the understanding of the VKS dynamo. This triggered several studies and some understanding of the role of ferromagnetic boundary conditions has been gained with the help of modeling and numerical simulation (see [25] for instance and references therein). Nevertheless the complexity of the VKS experiment makes the full understanding far from perfect. The future developments of the experimental configuration are aimed at finding the simplest configuration (both from the technical and physical point of view) with dynamo generation so that more detailed measurement and modeling can be implemented.

2.3.6 Low dimensional dynamics of the magnetic field

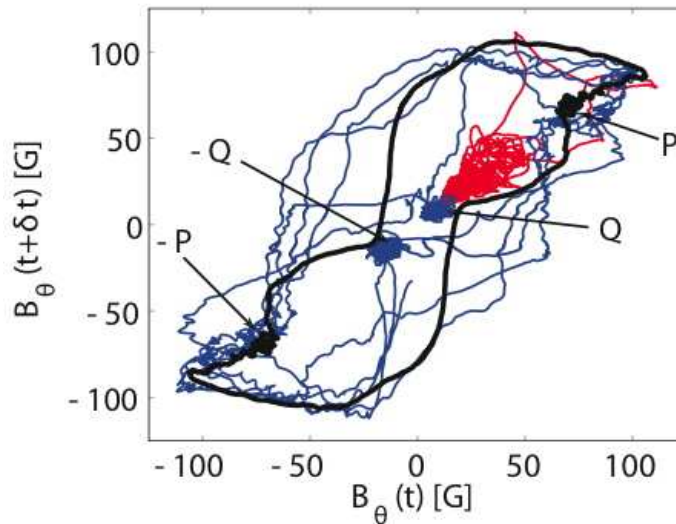


Figure 23: Plot of a cut in a phase space reconstruction $[B_\theta(t), B_\theta(t + \delta t)]$ with $\delta t = 1$ s for three regimes: in black for reversals, the magnetic field being rescaled by an ad-hoc factor accounting for the fact that the probe location is not in the mid-plane. In blue, for symmetric bursts ($F_1 = 21$ Hz, $F_2 = 15$ Hz, $\Theta = 0.17$) and in red for asymmetric bursts ($F_1 = 22$ Hz, $F_2 = 15$ Hz, $\Theta = 0.19$). In these last two plots the magnetic field is time averaged over 0.25 s to remove high frequency fluctuations. Figure from [31].

Another striking feature of the VKS dynamo lies in the robustness of the phase space trajectories as shown in figure 23. Three dynamical regimes in a very narrow region of the parameter space are shown. The trajectory corresponding to reversals shown above (black) show the stationary phase (P and $-P$) linked with a very reproducible trajectory (averaged here) that points out also two specific points (Q and $-Q$). A small change in parameters changes the dynamical regime into bursts (red) from the Q point. Another small change in parameters modifies the dynamics into a chaotic exchange between the P, $-P$, Q and $-Q$ points. These features are reminiscent of low dimensional dynamical systems (with noise) and the trajectories could be interpreted as heteroclinic orbits connecting unstable points (with both stable and unstable directions). The variety of dynamical regimes correspond to a region

of the parameter space where the stable points P or Q change their character from stable (stationary dynamo) to unstable (dynamical dynamo). Other similar examples of low dimensional behaviors in VKS are described in [31, 5, 51, 3]

This low dimensional dynamics is quite surprising when considering high level of turbulence (the Reynolds number is over 10^6). Nevertheless the role of the turbulent fluctuations seems to be restricted to introducing a relatively limited amount of noise in the deterministic low dimensional interactions between four nearly critical dynamo modes. This may be due to the moderate magnetic Reynolds number that may be insensitive to the fastest time scales of the turbulent fluctuations resulting in a rather low effective amount of noise.

This low dimensional dynamics has been interpreted by Pétrélis & Fauve as the interaction of two modes nearly critical with opposite parity under a symmetry of the experiment (e.g. dipole and quadrupole) and this interpretation has also been proposed for the reversals of the Earth magnetic dipole [46]. The similarity between the observed behavior of the VKS dynamo and that of the Earth (and possibly the sun) is one of the very stimulating result of the VKS collaboration.

The gallium experiment is a step in the understanding of the saturation of the dynamo in VKS. Nevertheless much remains to be understood in the VKS dynamo. Once a convenient configuration of the VKS dynamo will be chosen, measurements with a higher number of probes have to be implemented to get a more detailed knowledge of the geometry of the dynamo field. Measurements of the velocity either by ultrasound or by potential probes would give some information on the modification of the flow by the dynamo field. Although the gallium experiment showed weak correlation between the magnetic field and the velocity, such simultaneous measurements may also be of help to understand the induction mechanism in VKS and in particular the role of the turbulent fluctuations.

3 Wave turbulence

Wave turbulence shares many features with hydrodynamical turbulence (out of equilibrium system with a large number of degrees of freedom, energy cascade...). A major difference lies in the existence of a statistical solution in the limit of weak non linearity. This limit makes no sense in hydrodynamical turbulence which is intrinsically strongly non linear.

The existence of the so-called Weak Turbulence Theory (WTT) for wave turbulence provides a clear understanding of the mechanism of energy transfer of the Kolmogorov-Zakharov spectral energy cascade. A closed kinetic equation for the spectral energy density can be derived. Stationary solutions have been exhibited for out of equilibrium situations: the Kolmogorov-Zakharov spectra (see for example [44] for a review). These solutions correspond to a constant flux of energy across wavenumbers and are reminiscent of the Richardson energy cascade in hydrodynamical turbulence. Here the energy transfer occurs through multiwave resonances (3 or more waves). The WTT formalism can go beyond spectra and also provides theoretical predictions of wave amplitude distributions and many other statistical quantities [13].

The theory was applied to a large variety of systems [44]: optics in non linear media, superfluids, water surface waves, atmospheric internal waves, sound, MHD, plasmas... The output is often restricted to spectral predictions. Furthermore few laboratory experiments were designed to test advanced predictions of the theory except for fluid gravity or capillary surface waves (see [20] for instance). The theory was recently applied to bending waves in thin elastic plates [19]. After the preliminary work of P. Lancien (ATER in our group), I built an experiment devoted to the study of this system. The use of high speed 2D profilometry gives access to a fully resolved (in space and time) measurement of the waves and opens the possibility to analyse more complex quantities than just the spectrum. I will first review the theoretical predictions of Düring, Rica & Josseland [19], then I will describe the experimental setup and show some very recent experimental results.

3.1 The Weak Turbulence Theory applied to thin elastic plates.

The equation of evolution of the deformation $\zeta(x, y, t)$ of an initially flat surface are the Föppl-Von Kármán equations:

$$\frac{\partial^2 \zeta}{\partial t^2} = -\frac{Eh^2}{12\rho(1-\sigma^2)}\Delta^2\zeta + \{\zeta, \chi\} \quad (18)$$

$$\frac{\rho}{E}\Delta^2\chi = -\frac{1}{2}\{\zeta, \zeta\} \quad (19)$$

where the $\{.,.\}$ operator is $\{f, g\} = f_{xx}g_{yy} + f_{yy}g_{xx} - 2f_{xy}g_{xy}$. E is Young's modulus, h the thickness of the plate, ρ its density and σ the Poisson ratio. χ is the stress function. The last term of the rhs of (18) is non linear and it is cubic in ζ . In the linear limit, (18) provides a dispersion relation

$$\omega_k = \sqrt{\frac{Eh^2}{12\rho(1-\sigma^2)}}k^2. \quad (20)$$

The linear wave propagation is due to the bending of the plate. The non linearity comes from the stretching of the plate by strong deformations.

In the WTT, a weak non linearity of the wave is assumed that allows for an asymptotic expansion. The object of study is the amplitude of Fourier modes of wave vector \mathbf{k} of amplitude k : here $\zeta_k(t) = \frac{1}{2\pi} \int \zeta(\mathbf{r}, t)e^{i\mathbf{k}\cdot\mathbf{r}}d^2\mathbf{r}$. The Föppl-Von Kármán equations can be rewritten

$$\rho\frac{\partial^2 \zeta_k}{\partial t^2} = -\rho\omega_k^2\zeta_k - \int V_{-k, k_2; k_3, k_4}\zeta_{k_2}\zeta_{k_3}\zeta_{k_4}\delta^{(2)}(\mathbf{k} - \mathbf{k}_2 - \mathbf{k}_3 - \mathbf{k}_4)d^2\mathbf{k}_{234} \quad (21)$$

with

$$V_{12;34} = \frac{E}{2(2\pi)^2} \frac{|\mathbf{k}_1 \times \mathbf{k}_2|^2 |\mathbf{k}_3 \times \mathbf{k}_4|^2}{|\mathbf{k}_1 + \mathbf{k}_2|^4} \quad (22)$$

The impulsion is defined as $p_k(t) = \rho\partial_t\zeta_k(t)$ and a canonical change of variable is introduced by Düring et al. [19] to exhibit the hamiltonian structure of the problem. $\zeta_k(t) = \frac{X_k}{\sqrt{2}}(A_k + A_{-k}^*)$ and $p_k = -\frac{i}{\sqrt{2}X_k}(A_k - A_{-k}^*)$, with $X_k = 1/\sqrt{\omega_k\rho}$ so that the evolution equation is

$$\frac{dA_k}{dt} = -i\omega_k A_k + iN_3(A_k), \quad (23)$$

where N_3 is the cubic non linear term. A time scale separation is assumed between the wave period $1/\omega_k$ and the non-linear evolution time scale so that A_k can be written

$$A_k(t) = a_k(t)e^{i\omega_k t} \quad (24)$$

where $a_k(t)$ is a slowly varying amplitude that can evolve on time scales intermediate between the wave period and the non linear time scale. The evolution of the amplitudes a_k is then described by

$$\frac{da_k^s}{dt} = -is \sum_{s_1 s_2 s_3} \int J_{-\mathbf{k}\mathbf{k}_1\mathbf{k}_2\mathbf{k}_3} e^{it(s\omega_k - s_1\omega_{k_1} - s_2\omega_{k_2} - s_3\omega_{k_3})} a_1^{s_1} a_2^{s_2} a_3^{s_3} \delta^{(2)}(\mathbf{k}_1 + \mathbf{k}_2 + \mathbf{k}_3 - \mathbf{k}) d^2\mathbf{k}_{123} \quad (25)$$

with $s_i = \pm 1$ (see [19] for details on notations). The next step of the procedure is to look for the evolution of the successive moments of a_k . The fast dynamics is expected to drive the system close to Gaussian statistics so that the successive moments can be expressed from the second order moment (the spectrum)

$$\langle a_{k_1} a_{k_2}^* \rangle = n_{\mathbf{k}_1} \delta^{(2)}(\mathbf{k}_1 + \mathbf{k}_2). \quad (26)$$

Finally, the spectrum follows a kinetic equation

$$\begin{aligned} \frac{dn_k^s}{dt} = 12\pi \int |J_{\mathbf{k}\mathbf{k}_1\mathbf{k}_2\mathbf{k}_3}|^2 \sum_{s_1 s_2 s_3} n_{\mathbf{k}_1} n_{\mathbf{k}_2} n_{\mathbf{k}_3} n_{\mathbf{k}} \left(\frac{1}{n_{\mathbf{k}}} + \frac{s_1}{n_{\mathbf{k}_1}} + \frac{s_2}{n_{\mathbf{k}_2}} + \frac{s_3}{n_{\mathbf{k}_3}} \right) \delta(\omega_k + s_1\omega_{k_1} + s_2\omega_{k_2} + s_3\omega_{k_3}) \\ \times \delta^{(2)}(\mathbf{k} + s_1\mathbf{k}_1 + s_2\mathbf{k}_2 + s_3\mathbf{k}_3) d^2\mathbf{k}_{123} \end{aligned} \quad (27)$$

which rhs term can be interpreted as a collision term between four resonant waves as expected from the cubic non linearity. This kinetic equation conserves the total momentum $\mathbf{P} = h \int \mathbf{k} n_{\mathbf{k}}(t) d^2 \mathbf{k}$ and the total energy $\mathcal{E} = h \int \omega_{\mathbf{k}} n_{\mathbf{k}}(t) d^2 \mathbf{k}$. For 4-wave interaction, it is in principle possible to conserve the wave action $\mathcal{N} = \int n_{\mathbf{k}}(t) d^2 \mathbf{k}$. In this specific case however, it is not possible due to the existence of a resonance $3 \leftrightarrow 1$ which does not conserve the particle number. This prevents the occurrence of an inverse cascade of action as can be observed in other 4-wave interacting systems.

Two kinds of stationary solutions can be exhibited in WTT. Rayleigh-Jeans equilibrium solutions of energy equipartition ($n_{\mathbf{k}} = T/\omega_{\mathbf{k}}$) are characterized by a zero flux of energy across scales. Out of equilibrium solutions with finite non zero flux of energy are usually looked for as $n_{\mathbf{k}} \propto \omega_{\mathbf{k}}^{-\alpha}$ and exhibited thanks to the homogeneity properties of the collision kernel in the kinetic equation. In our specific case however, $\alpha = 1$ which corresponds to the zero flux solution (degeneracy of the Rayleigh-Jeans spectrum) so that logarithmic corrections have to be introduced. Düring *et al.* predict the following form for the out of equilibrium spectra of the deformation:

$$E_{\zeta}(k) = C \frac{P^{1/3}}{(12(1 - \sigma^2))^{1/6}} \frac{\ln^{1/3}(k^*/k)}{\sqrt{E/\rho} k^3} \quad (28)$$

where C is a dimensionless constant and P is the energy flux. The spectrum is proportional to $P^{1/3}$ as expected from a 4-wave interaction. The logarithmic correction to the power law in k requires the introduction of a cutoff wavenumber k^* (or frequency $\omega^* = \omega_{k^*}$).

Experimentally it is often easier to measure the wave amplitude in a single point. The only spectrum available is then a frequency spectrum. For the plate, experiments provide rather the velocity spectrum $E_v(\omega)$. The prediction for the space spectrum is then translated into frequency space through the dispersion relation $\omega \propto k^2$. It gives:

$$E_v(\omega) = C' \frac{hP^{1/3}}{12(1 - \sigma^2)} \ln^{1/3}(\omega^*/\omega). \quad (29)$$

In many other physical systems it is possible to predict the scaling of the expected spectrum by dimensional analysis [16]: one takes for granted the P scaling of the spectra as $P^{1/(N-1)}$ where N is the number of waves in resonance. The only relevant dimensional parameter is assumed to be the coefficient λ involved in the dispersion relation $\omega = \lambda k^\beta$. Under these assumptions the spectrum is uniquely constrained. In our case, this reasoning is not valid as the equation of motion involves three dimensionless parameters to estimate the spectrum: for instance $E_v/(h\sqrt{E/\rho})$, $P^{1/3}/(h\omega)$ and $P(\rho/E)^{3/2}$. In other words $\lambda = h\sqrt{E/(12(1 - \sigma^2)\rho)}$ is not the only relevant dimensional parameter but E (or h) must also be taken into account [34]. The result of dimensional analysis can be stated for instance as

$$E_v(\omega) = h\sqrt{\frac{E}{\rho}} g \left(\frac{P^{1/3}}{h\omega}, P \left(\frac{\rho}{E} \right)^{3/2} \right). \quad (30)$$

By comparing with (29), it is tempting to conclude that the cutoff frequency should scale as $\omega^* \sim P^{1/3}/h$.

3.2 Description of the experimental setup

The experimental setup is quite simple (figure 24). A steel plate $2 \times 1 \text{ m}^2$, 0.4 mm thick is held vertically. An electromagnetic vibrator is anchored 40 cm from its bottom and shakes the plate by vibrating horizontally at 30 Hz. In all experiments reported here, the only control parameter is the amplitude of the forcing.

Two experimental techniques have been implemented. First, I used a Laser vibrometer which measures either the normal velocity of the plate in a single point or the velocity difference over two points [34]. The measurement point(s) can be scanned over the plate surface.

Another technique was brought to me by P. Cobelli *et al.* [14] from their nearby laboratory in ESPCI. It is a Fourier transform profilometry (FTP) technique which can measure the deformation of a surface

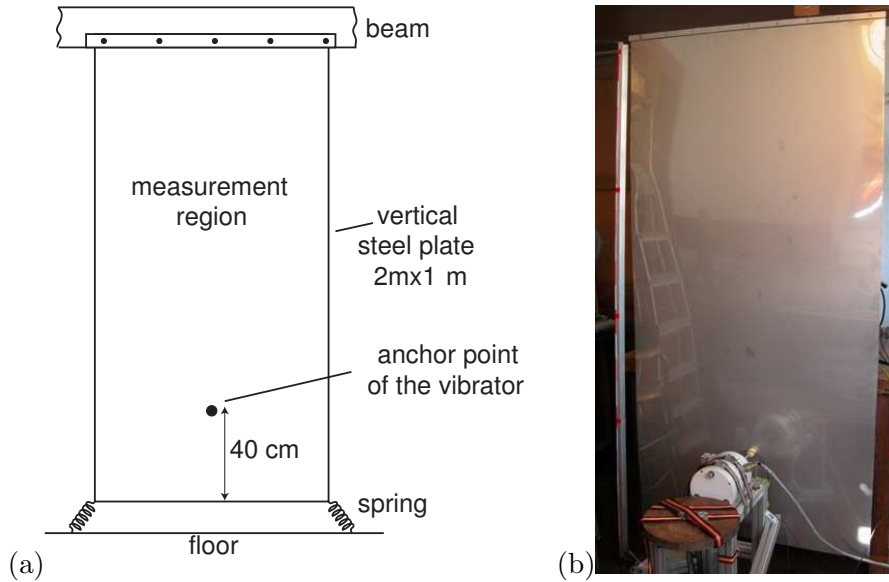


Figure 24: Sketch (a) and picture (b) of the wave turbulence experiment. Figure (a) from [34].

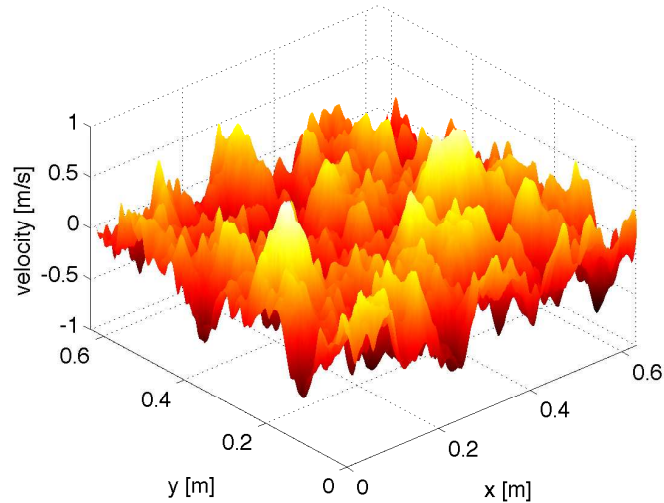


Figure 25: Example of the normal velocity of the plate using the FTP technique. Figure from [15].

on a significant portion of the plate. When coupled with a high speed camera, this technique provides a movie of the deformation of the plate resolved in time and space. The principle is the following: a videoprojector projects a sine intensity pattern onto the plate (painted in matte white). When recorded by the camera, the pattern is phase modulated by the deformation of the plate [14]. The demodulation of the successive pictures provides a temporal measurement of the deformation. The normal velocity field of the plate is obtained from the difference between successive demodulated pictures. A snapshot of the velocity is shown in figure 25.

3.3 Observation of wave turbulence in a thin elastic plate

3.3.1 Wave turbulence

Spectra of the velocity field $v(\mathbf{r}, t)$ are shown in figure 26. (a) shows the full space-time spectrum $E_v(\mathbf{k}, \omega)$. The energy is concentrated on a surface which seems to be of cylindrical symmetry around the frequency axis. This confirms that the motion of the plate is made of waves, the energy of which is concentrated

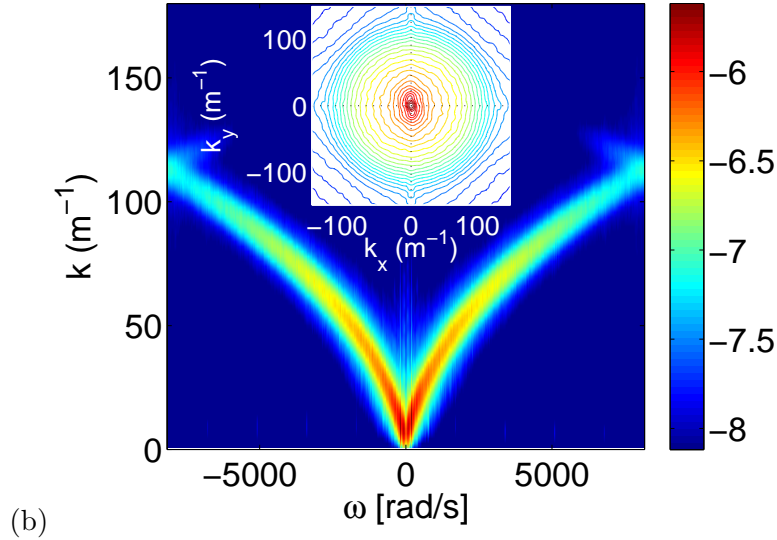
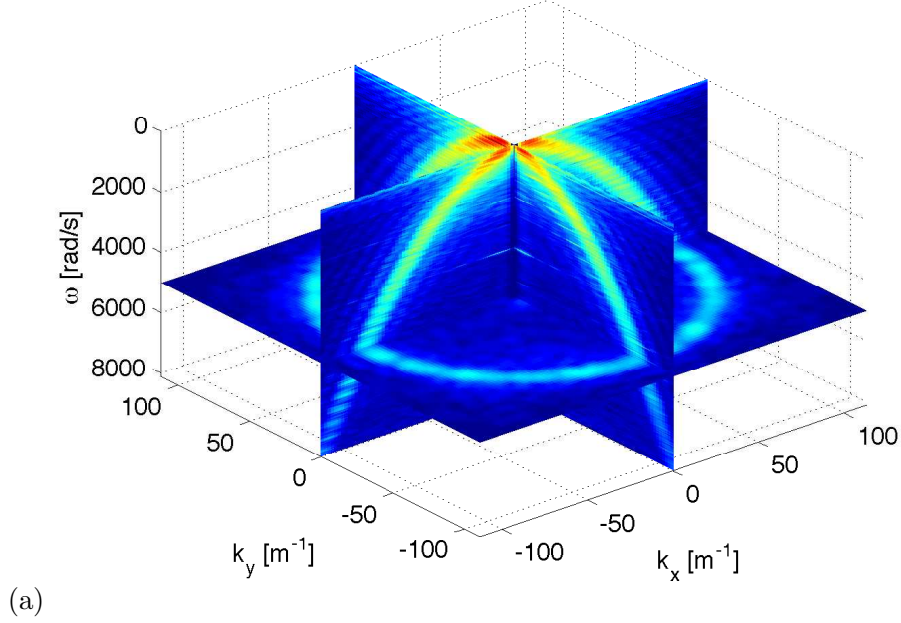


Figure 26: (a) Space-time spectrum $E_v(\mathbf{k}, \omega)$ of the deformation velocity of the plate. Measurement by the FTP technique. Colors are log-scaled. (b) Space-time spectrum $E_v(k, \omega)$ averaged over directions of \mathbf{k} . Colors are log-scaled. Inset: contours of the space spectrum $E_v(\mathbf{k})$ integrated over the frequencies (i.e. averaged in time). Figures from [15].

on a surface representing the dispersion relation (close to $\omega \propto \mathbf{k}^2$). The direction integrated spectrum $E_v(k, \omega)$ is shown in figure 26(b) and shows again that the energy is concentrated on a line in the (k, ω) plane and that the spectrum is relatively isotropic in the \mathbf{k} space. It is better seen in the inset of figure 26(b) where the contours of $E_v(\mathbf{k})$ are circles except at low wavenumbers at which the anisotropy of the forcing and the plate is visible. This is a convincing confirmation that the motion of the plate is a wave turbulence.

Although the previous results are spectacular, similar information was provided in a slightly less direct way by two point differential measurements by Laser profilometry which is both less expensive and easier to implement with a commercial equipment [34]. The Laser profilometer measures the normal velocity difference $\delta v(x, t) = v(x, t) - v(0, t)$ of two points separated by a distance x . It is possible to scan a collection of positions x (but not simultaneously though). A Fourier analysis can be performed in the time domain to get $\delta v(x, \omega)$. Following the WTT, one can assume that $\delta v(x, \omega)$ is due to the

superposition of waves at the frequency ω and propagating isotropically in all direction of $\mathbf{k}(\omega)$. This can be written as

$$\delta v(x, \omega) = e^{-i\omega t} \int A(\theta, \omega) (e^{ik \cos \theta x} - 1) k d\theta \quad (31)$$

where θ is the angle of \mathbf{k} . As in the WTT we assume that there is no two-wave correlation between two distinct angles of propagation so that

$$\langle A(\theta, \omega) A^*(\theta', \omega) \rangle = \langle |A(\omega)|^2 \rangle \delta(\theta - \theta'). \quad (32)$$

It follows that the velocity difference power spectrum density can be written simply as

$$E_{\delta v}(x, \omega) = 2E_v(\omega)(1 - J_0(kx)) \quad (33)$$

where J_0 is the 0-th order Bessel function. The spatial dependence of $E_{\delta v}(x, \omega)$ is expected to be a Bessel function which scaling parameter is the wavenumber and which amplitude is the single point velocity spectrum.

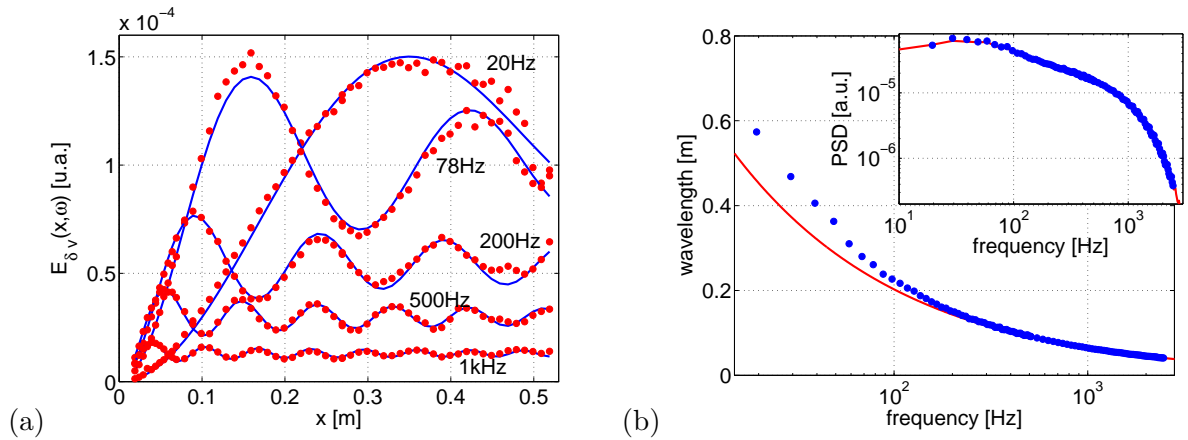


Figure 27: (a) Spatial evolution of $E_{\delta v}(x, \omega)$ for 5 values of ω . The dots are experimental data and the blue lines are fits of the J_0 Bessel function. (b) Parameters of the fit in (a) (scaling factor and amplitude). Main plot: dots are the scaling parameter displayed as wavelength and the line is the dispersion relation of the linear waves. Inset: amplitude of the J_0 function (dots) compared to the single point spectrum (red line). Figures from [34].

Among the quantities present in equation (33) above, $E_{\delta v}(x, \omega)$ has been measured for a collection of x and $E_v(\omega)$ can be measured independently with single point profilometry at the same positions. A J_0 function can be fitted to $E_{\delta v}(x, \omega)$ with two parameters, a scaling factor and an amplitude that can be compared to k and $E_v(\omega)$ respectively. The result is presented in figure 27. It is seen that the amplitude factor is in remarkable agreement with $E_v(\omega)$ and the scaling factor is close to the linear dispersion relation except at low frequency. These observations validate the hypothesis of isotropic superposition of waves with a dispersion relation close to the linear one. It shows again that the motion of the plate is due to wave turbulence.

3.3.2 Weak turbulence ?

The one point spectrum is shown in figure 29. The theoretical prediction is the blue dashed line and is seen to disagree with the measured spectra. The latter show rather a power law decay over a decade with an exponent in the range $[-0.6, -0.5]$ followed by an exponential decay at high frequencies. From the exponential decay, one can extract a cutoff frequency ω^* which is seen to scale as $P^{1/3}$ as expected from dimensional analysis (here P is measured directly as the mechanical power injected by the vibrator). The disagreement with the theory together with the confirmation that the motion is nevertheless a turbulence of waves suggests that another process is perturbing the overall picture of the WTT. Strong linearities could be responsible or possibly dissipation could interact with the cascade.

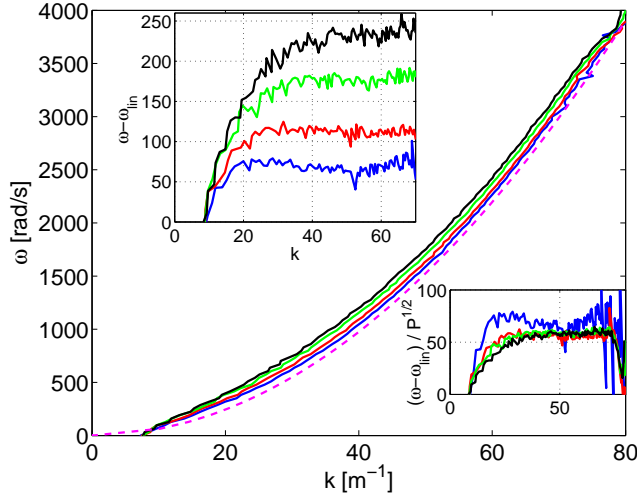


Figure 28: Dispersion relation obtained by extracting the maximum of energy at each frequency in figure 26(b). The pink dashed line is the linear dispersion relation. Blue, red, green and black correspond to forcing amplitudes 1, 2, 3 and 4 V respectively. Top inset: frequency shift between the observe dispersion relation and the linear one. Bottom inset: frequency shift normalized by $P^{1/2}$. Figures from [15].

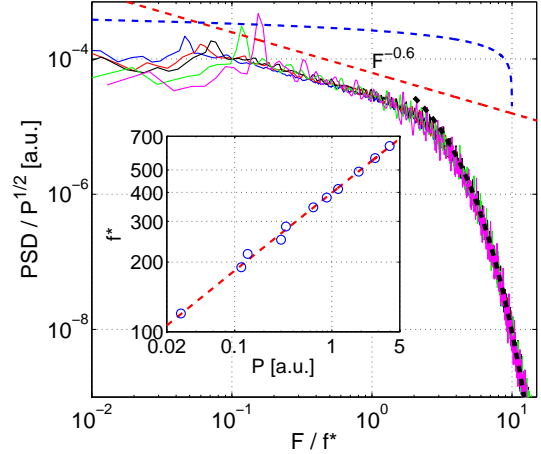


Figure 29: One point spectrum measured by Laser Doppler profilometry. Thin solid lines: measured spectra for various forcing amplitude. Red dashed line $1/F^{0.6}$ scaling. Blue dashed line, $\ln(10f^*/F)^{1/3}$. Black dashed line: exponential decay. Inset: measured f^* as a function of the input power. Figure from [34].

The dispersion relation can be extracted from the spectrum by measuring the position of the crest of maximum energy in figure 26(b) for instance. The result is shown in figure 28 for various forcing amplitudes and compared to the dispersion relation of linear waves. A small but clear shift is observed. Such a shift is expected as a first perturbative correction to the linear waves in the WTT theory [44]. In our experiment, the WTT prediction cannot be used as the WTT is expected to be incorrect from the observation of the spectrum. Nevertheless, in the WTT the frequency shift to the dispersion relation is expected to have the same scaling in P as the spectrum. Here the scaling exponent of the frequency shift is close to $P^{1/2}$ which collapse quite well the frequency shift (in contrast to $P^{1/3}$). The spectrum is also scaling with an exponent close to $1/2$. It suggests that some formal aspects of the WTT may still be valid. The fact that the frequency shift is small also suggests that the non-linearity is small. It discards the hypothesis of strong linearity to explain the disagreement of the measured spectrum with the WTT prediction. Recent numerical simulations by C. Josserand have shown that introducing a more realistic dissipation in the simulation of the Föppl-Von Kármán equation significantly alters the shape of the spectra. The simulated spectra resemble at least qualitatively the measured spectra. Thus dissipation is expected to play a role in the dynamics of the energy cascade that may be leaking energy as it processes down to smaller scales.

The WTT can provide more predictions than just spectra. For instance it predicts the shape of the distribution of the magnitude of the wave amplitude $|A_k|$ [13]. It is predicted to be close to a Rayleigh (exponential) distribution. Departure from the exponential is expected as higher order corrections due to the finite (weakly non linear) amplitude of the wave. Figure 30 shows an preliminary example of the distribution of the wave amplitude. The distribution is indeed close to exponential. If any departure to exponential exists then much more statistics seem required in future work. The hypothesis of quasi-gaussian distribution of the amplitude seems to be valid for the plates. Note that no intermittency of the velocity space or time increment distribution was observed which is consistent with this observation.

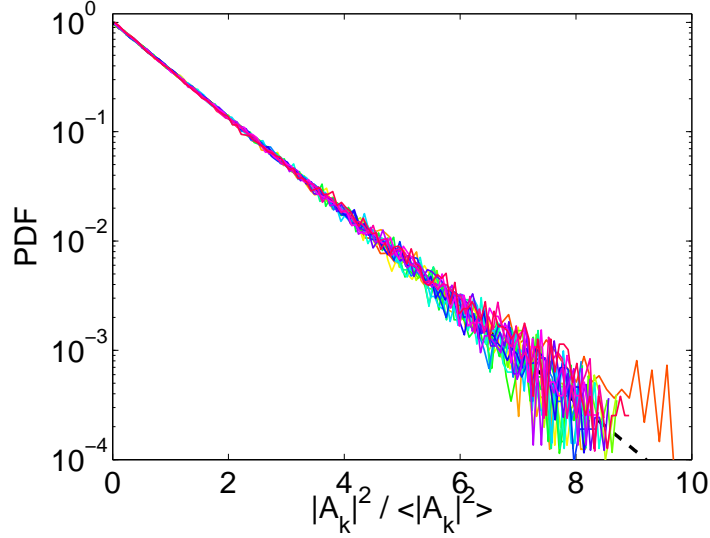


Figure 30: PDF of the amplitude $|A_k(t)|^2$ for various values of the wavenumber ($k/2\pi = 1/\lambda = 1.37, 4.11, 6.85, 9.59, 12.3, 15.1, 17.8, 20.5, 23.3 \text{ m}^{-1}$). The dashed line is an exponential distribution. The forcing corresponds to $1/\lambda = 2.8$.

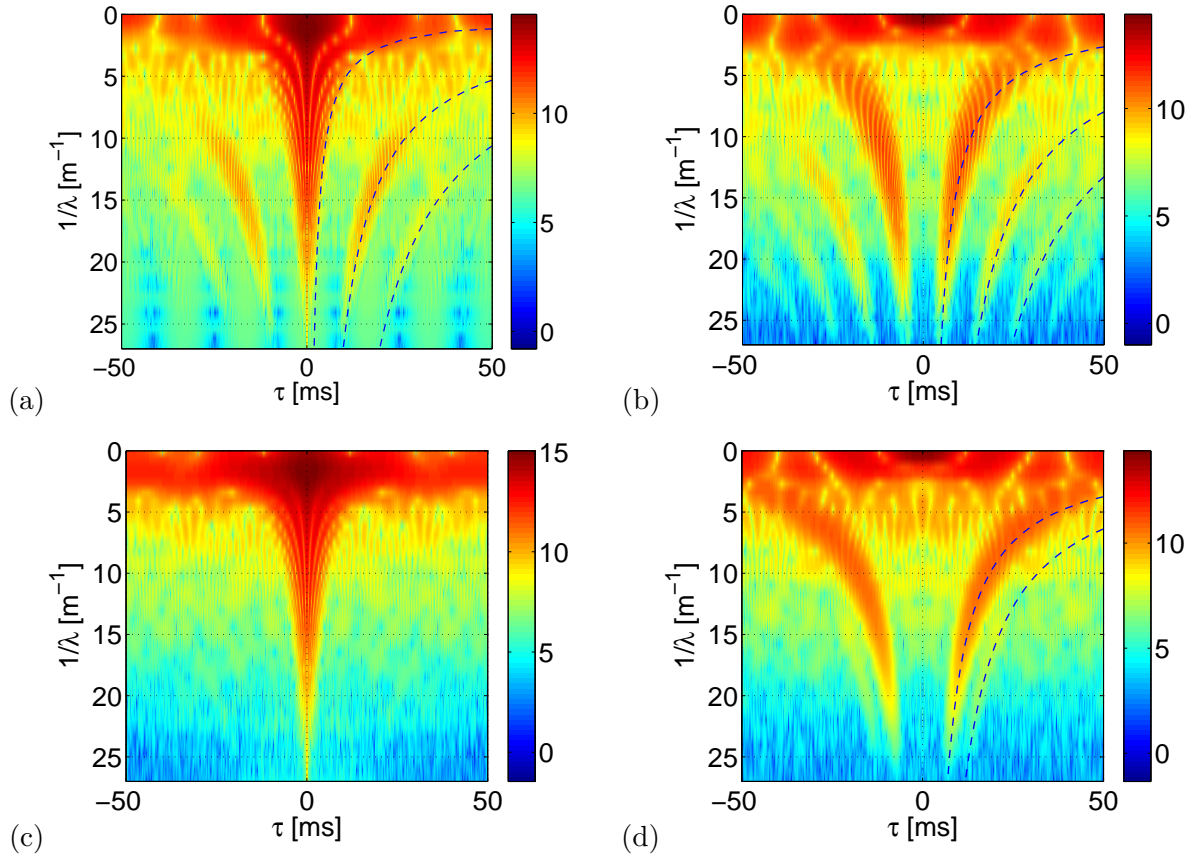


Figure 31: Autocorrelation $C_{k,k}(\tau)$ of $A(\mathbf{k}, t)$ and cross correlation $C_{k,-k}(\tau)$ of $A(\mathbf{k}, t)$ and $A(-\mathbf{k}, t)$ for horizontal or vertical \mathbf{k} (color code is log scaled). Dashed lines are time of flights computed using the group velocity of the linear dispersion relation over some given distances D . (a) $C_{k,k}$ for horizontal \mathbf{k} . $D = 0.4, 2$ and 4 m . (b) $C_{k,-k}$ for horizontal \mathbf{k} . $D = 1, 3$ and 5 m . (c) $C_{k,k}$ for vertical \mathbf{k} . (d) $C_{k,-k}$ for vertical \mathbf{k} . $D = 1.4, 2.4 \text{ m}$.

3.4 Wave packet billiard

When computing $A(\mathbf{k}, t)$ by Fourier transform of the deformation of the plate, the resolution δk in k space is imposed by the size L of the picture, roughly as $\delta k = 2\pi/L$. The motion being a wave, this resolution

is translated into frequency resolution $\delta\omega$ by the dispersion relation ($\omega = Ck^2$): $\delta\omega = 2Ck\delta k = v_g\delta k$ where $v_g = \frac{d\omega_k}{dk}$ is the group velocity. It means that $A(\mathbf{k}, t)$ is actually the amplitude of a wave packet of extension $2\pi/\delta\omega = L/v_g$ in time. To check this fact, I computed the autocorrelation of $A(\mathbf{k}, t)$ as shown in figure 31(a,c) for horizontal and vertical \mathbf{k} . The envelop of the autocorrelation is seen to have a width corresponding to a propagation distance 35 cm which corresponds to the effective width of the image when using a Hanning windowing. Secondary lobes can be observed for higher τ in figure 31(a) (horizontal \mathbf{k} or direction of propagation). They correspond to propagation distances 2 and 4 m (recall that the plate is 1 m wide horizontally and 2 m tall). The cross-correlation of $A(\mathbf{k}, t)$ and $A(-\mathbf{k}, t)$ (i.e. a wave packet propagating in the opposite direction) show no correlation at $\tau = 0$ but some shifted peaks at propagation distances 1, 3 and 5 m. These peaks correspond to rebounds of the wave packet on the boundary of the plate. $D = 1$ m is the distance travelled by the wave packet with one rebound until it comes back to the center of the image with the opposite direction. $D = 2$ m is the distance traveled by the packet after 2 rebounds until it comes back with the same direction at the center of the image. The successive peaks observed in figure 31(a,b) are the successive passage times of a wave packet when traveling horizontally and bouncing on the sides of the plate.

The first rebound is clearly visible, the next rebounds are very faint due to dissipation or to energy transfer to other values of k . The fast damping of the energy of the rebounds suggests that the quality factor of the reflecting cavity is very low. For this reason, I do not expect that discretization of modes due to the finite size of the plate is relevant here. The spectral width of the mode must be very large due to the low quality factor that no mode selection must operate here. From this point of view, one can consider that the effective size of the plate is infinite.

For vertically propagating wave packets (figure 31(c,d)), the observations are quite different. No rebound is visible on $C_{k,k}$. Two rebounds are visible on $C_{k,-k}$: the first is very clear and corresponds to $D = 1.4$ m. It is the rebound on the top of the plate. The second rebound is barely visible and corresponds to $D = 2.4$ m. This corresponds to a rebound in the lower part of the plate which is most likely strongly perturbed by the anchoring of the vibrator. The wave packets must be scattered in other directions so that it is no more visible here. The rebound is strongly damped by this scattering process and also by the twice longer distance to travel before coming back. This is why no 2-rebounds peaks are visible in figure 31(c).

The FTP technique allows to measure the deformation of the plate resolved in time and space. It opens the way to comparison to more elaborate quantities as simply the spectrum. The above observations show that even though the WTT is defective at predicting the spectrum, other quantities seem to validate some other formal aspects of the theory. For example the distribution of the amplitude of the wave $|A_k|$ is close to gaussian as expected in the WTT. Further analysis of the experimental (and numerical) data must be conducted in close collaboration with theoreticians. I expect some progress in the theoretical approach of wave turbulence from such a close collaboration. The premise of the WTT as applied to the thin plate, must be changed most likely to take into account dissipation.

Conclusions

My personal contribution to the advancement of the understanding of the various fields described above is mostly experimental and I had the opportunity for most of my work to remain in close contact with colleagues in theory or numerics. This provided a fruitful interaction that allowed the experimental results to be quickly integrated in the common progress of each field.

The study of turbulence entered in a new dynamics in the last decade boosted by the development of new experimental techniques in Lagrangian studies in parallel to numerics. The development of the Doppler techniques and the fast technical progress in high speed cameras pave the way to resolved measurements of particles dynamics in highly turbulent flow. The ultrasound Doppler technique provided the first inertial range data of the Lagrangian dynamics. I contributed to the gathering of Lagrangian acceleration data by joining the group of E. Bodenschatz in Cornell to develop further the silicon strip

detectors. These unique detectors were the only ones at the time to provide such a time resolution. With Romain Volk, we developed a Laser Doppler technique which provides the same resolution and we were able to study experimentally for the first time the acceleration of inertial particles. All these experimental observations open the way to a better modeling of the small scales of turbulence in numerical codes for simulation of practical problems in turbulent transport.

Homogeneous and isotropic turbulence is in many ways a theoretician toy. In many flows of practical concern, the statistics is neither homogeneous and isotropic. Therefore I think that all the technology developed for Lagrangian tracking should be turned also to the study of boundary layer flows in particular. These are of strong interest in mechanical or environmental issues. The typical laboratory experiment could be a water tunnel that is actually present in many mechanical engineering departments. In a boundary layer, the distribution of Lagrangian velocity is not constraint to be identical to that of the Eulerian velocity. In particular, one expects particles to move away from the walls on average even though the average flow is parallel. Even though 3D particle tracking with several cameras is clearly the most adapted technique, the Laser Doppler technique could provide also some information on the evolution of the accelerations statistics as a function of the distance from the wall. The new Lagrangian data would be especially useful to calibrate stochastic models of particle dispersion in shear flows, which parameters are at best weakly constrained so far. Such models are widely used for LES modeling of atmospheric transport for instance.

I had no contribution in the design of the VKS2 experiment because I joined the group once the setup was almost ready to run. But I contributed to the data acquisition and analysis of most experimental runs of VKS2 and to the choice (always strongly debated) of the modifications of the experimental setup. I think that the VKS experiment plays a major role in the understanding of magnetic field generation and of the dynamics of the Earth magnetic field. The instrumentation tested in the Gallium experiment in Paris as well as in similar experiments in Lyon, could be implemented in VKS to get some insight of the induction mechanism leading to the dynamo. The ω -effect induction is clearly at work here but the second step is largely hypothetical so far even if it is supported by numerical models. Even the geometry of the dynamo field is still quite hypothetical as the number of magnetic probes is limited. The development of further instrumentation in VKS is planned in the near future. Nevertheless, as noted above, the role of turbulence in VKS seems to be restricted to ensure that symetries of the flow are broken so that to circumvent Cowling's theorem and to introduce a small amount of noise to trigger the reversals of the magnetic field for instance. This may come from the moderate value of the magnetic Reynolds number. To get much higher values of Rm is a real challenge in liquid metals as the required mechanical power raises tremendously with Rm . To gain an order of magnitude in Rm would require a dedicated hydraulic dam to provide enough power... The use of plasmas could be better suited. The large magnetic fields required to confine the plasma makes the study of the dynamo also problematic.

Concerning the wave turbulence, the use of the Fourier transform profilometry technique leads to a fully resolved measurement of the deformation of the thin plate on most of its surface. It opens the way to a vast ensemble of new measurements that will enable a detailed comparison with theoretical predictions and most likely a significant contribution to the theoretical progress. With E. Falcon and E. Herbert, we are currently adapting the same technique to turbulence of surface waves on water. These waves display several features that are distinct from the plates. First, two kinds of waves exist, capillary and gravity waves. The study of the crossover between the two is interesting even though it may be at the limit of the FTP technique. One major difference with the plates lies in the occurrence of strong linearities. These can be observed as crests and even breaking waves. The WTT theory concerns only weak non linearities. So gravity waves are good candidates to investigate the large non linearity limit and recent theoretical developments deal with this case. Wave turbulence is, at least from the experimental side, a open field of research with promising perspectives.

Acknowledgments

I am aware to have benefitted from constant very good working conditions either in Lyon, Cornell or currently in Paris. First during my PhD with J.-F. Pinton, I benefited from a unique technical staff including in particular P. Metz and M. Moulin who were extremely precious to me. Collaborating with theoreticians and “numericists” among which A. Arnéodo, J. Delour, L. Chevillard, E. Lévêque and O. Michel was very enriching to me. I benefited constantly from the neighborhood of the precious colleagues of the Laboratoire de Physique in ENS de Lyon.

When moving to Cornell, I found the same kind of very enriching scientific environment (let alone the natural environment of the Finger Lakes area which is great memories to me). Working with A. Crawford was a daily pleasure and I must thank also E. Bodenschatz for accepting me in his group and for continued collaboration over the recent years. Discussions with S. Pope, Z. Warhaft and L. Collins were extremely enriching also.

I would like to thank all my colleagues of the VKS collaboration for providing me the opportunity to contribute to this unique scientific experience. The observation of the dynamo is a great achievement. Even though we have encountered some non scientific difficulties, I must say that every new experimental result is fascinating.

I thank F. Pétrélis and S. Fauve, for the precious scientific environment in Ecole Normale Supérieure and also M. Berhanu for surviving as my first PhD student. Romain Basset did a impressive amount of work when tuning the freshly build active grid wind tunnel and fighting with cold wire measurement although his work is not directly represented here. Pierre Lancien was also a very pleasant person and had in particular the merit to understand how to have the Laser profilometer to measure something on metal plates. Julien Debray (engineer student) spent also a couple months working on the plates to try to understand the transition to wave turbulence. I thank the students of ENS to which I imposed to work on turbulence during lab courses and who stimulated me to build the wind tunnel or the reproduce the Lowes & Wilkinson dynamo for instance.

I am also grateful to P. Cobelli, P. Petitjeans, A. Maurel and V. Pagneux to share with me their FTP technique which is an extremely efficient tool. It opens a vast perspective of research in wave turbulence.

Finalemment je remercie très chaleureusement Pascale pour m’avoir supporté (au sens français et anglais) pendant toutes ces années et pour avoir relu courageusement ce manuscrit.

Appendix: Acoustic selective detection in a waveguide.

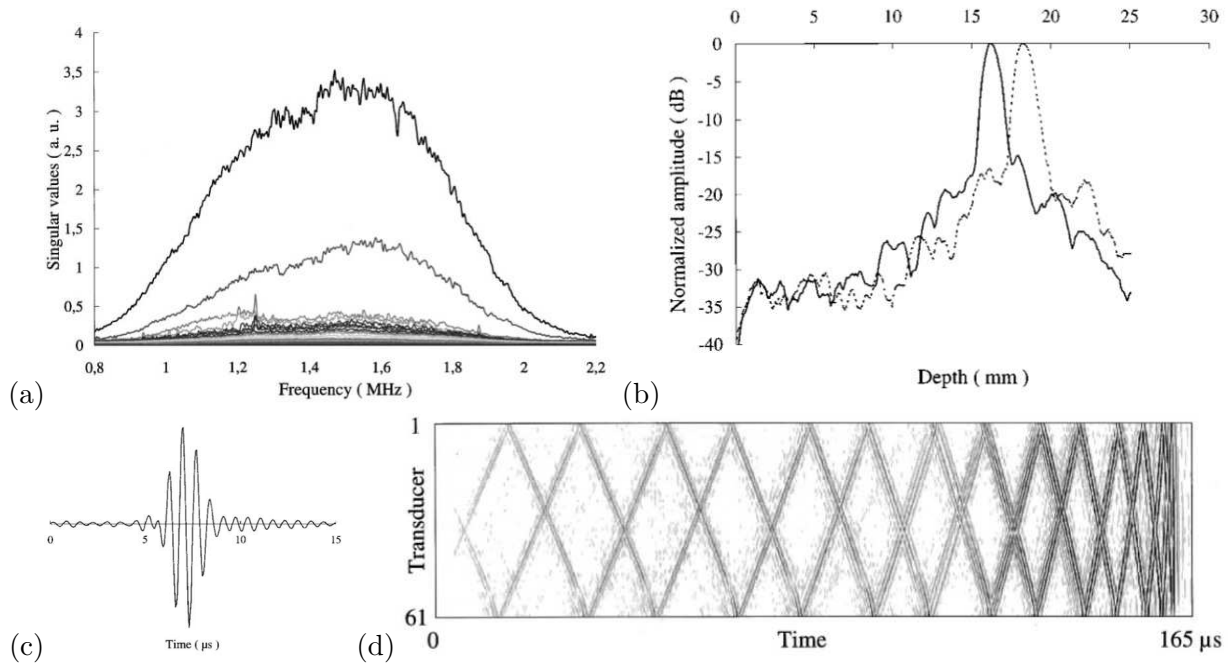


Figure 32: (a) singular values versus frequency, (b) amplitude measured in the vicinity of the targets after emitting the temporal signal (d) corresponding to each target, (c) temporal trace of the pressure field at the position of the wire, (d) temporal signal reconstructed from the first eigenvalue. See text and [43] for details.

I recall briefly here a research work independent from that reported above. I worked with C. Prada and M. Fink on the DORT (acronym for Decomposition of the Time Reversal Operator) method during my military draft as a scientist. The issue is the acoustic detection of a target in a waveguide (e.g. low depth ocean). It is modeled in the laboratory as the propagation of ultrasound in water confined between steel plates [43]. Ultrasound is emitted and received on a single array of transducers spanning the width of the waveguide.

The core of the DORT method is to build the transfer matrix \mathbf{K} . $k_{ij}(t)$ is the signal received by the transducer i after reflection on the targets when emitting a pulse by the transducer j . At each frequency ω , the component $K_{ij}(\omega)$ obtained by Fourier transform of $k_{ij}(t)$ allows us to build the transfer matrix $\mathbf{K}(\omega)$. A singular value decomposition of \mathbf{K} is performed at each frequency. The singular values are shown in figure 32(a) in the case of two targets. The relative amplitude of the singular values is related to the reflectivity of the targets. Here two targets of different reflectivities are placed at the same distance in the waveguide. The two largest singular values correspond to the echoes of the targets and the other values correspond to noise. At each frequency, the eigenvectors corresponding to the two largest eigenvalues can be interpreted as the complex amplitude that must be emitted by the array of transducers so that to focus selectively on the targets. Here, the guiding of the wave by reflection on the walls of the channel increases the focussing properties (thanks to the virtual images of the emitters) compared to the diffraction limit expected in open water [43].

By combining the eigenvectors at all frequencies, a temporal signal can be constructed for each transducer (figure 32(d)). The successive reflections on the wall are clearly visible. Emitting this signal allowed us to achieve a spatio-temporal specific focussing at the position of a target. The amplitude received in the plane of the target is shown in figure 32(b) and the temporal signal received on the first target is shown in (c). The duration of the pulse on the target is much shorter than the emitted signal due to simultaneity of the arrival of all reflected contributions. A clear focussing is achieved both in time and frequency. This method could be used for focused and selective underwater acoustic communication for instance.

References

- [1] Anand M.S. & Pope S.B. *Diffusion behind a line source in grid turbulence*, volume 4 of *Turbulent Shear Flows*, 46. Springer-Verlag, Berlin (1985).
- [2] Arnéodo A., Benzi R., Berg J., Biferale L., Bodenschatz E., Busse A., Calzavarini E., Castaing B., Cencini M., Chevillard L., Fisher R.T., Grauer R., Homann H., Lamb D., Lanotte A.S., Lévêque E., Lüthi B., Mann J., Mordant N., Müller W.C., Ott S., Ouellette N.T., Pinton J.F., Pope S.B., Roux S.G., Toschi F., Xu H. & Yeung P.K. “Universal intermittent properties of particle trajectories in highly turbulent flows”. *Phys. Rev. Lett.*, **100**(25), 254504 (2008).
- [3] Aumaitre S., Berhanu M., Bourgoïn M., Chiffaudel A., Daviaud F., Dubrulle B., Fauve S., Marié L., Monchaux R., Mordant N., Odier P., Pétrélis F., Pinton J.F., Plihon N., Ravelet F. & Volk R. “The VKS experiment: turbulent dynamical dynamos”. *C. R. Physique*, **9**, 689 (2008).
- [4] Beck C. “Dynamical Foundations of Nonextensive Statistical Mechanics”. *Phys. Rev. Lett.*, **87**(18), 180601 (2001).
- [5] Berhanu M. *Magnétohydrodynamique turbulente dans les métaux liquides*. Ph.D. thesis, Université Pierre et Marie Curie (2008).
- [6] Berhanu M., Gallet B., Mordant N. & Fauve S. “Reduction of velocity fluctuations in a turbulent flow of gallium by an external magnetic field”. *Phys. Rev. E*, **78**(1), 015302 (2008).
- [7] Berhanu M., Monchaux R., Fauve S., Mordant N., Pétrélis F., Chiffaudel A., Daviaud F., Dubrulle B., Marié L., Ravelet F., Bourgoïn M., Odier P., Pinton J.F. & Volk R. “Magnetic field reversals in an experimental turbulent dynamo”. *EPL*, **77**, 59001 (2007).
- [8] Bourgoïn M., Marié L., Pétrélis F., Gasquet C., Guigon A., Luciani J.B., Moulin M., Namer F., Burguete J., Chiffaudel A., Daviaud F., Fauve S., Odier P. & Pinton J.F. “Magnetohydrodynamics measurements in the von Kármán sodium experiment”. *Phys. Fluids*, **14**(9), 3046 (2002).
- [9] Calzavarini E., Volk R., Bourgoïn M., Lévêque E., Pinton J.F. & Toschi F. “Acceleration statistics of finite-sized particles in turbulent flow: the role of Faxen forces”. *J. Fluid Mech.*, **630**, 179 (2009).
- [10] Chevillard L. & Meneveau C. “Lagrangian Dynamics and Statistical Geometric Structure of Turbulence”. *Phys. Rev. Lett.*, **97**, 174501 (2006).
- [11] Chevillard L., Roux S.G., Lévêque E., Mordant N., Pinton J.F. & Arnéodo A. “Lagrangian Velocity Statistics in Turbulent Flows: Effects of Dissipation”. *Phys. Rev. Lett.*, **91**(21), 214502 (2003).
- [12] Chevillard L., Roux S.G., Lévêque E., Mordant N., Pinton J.F. & Arnéodo A. “Intermittency of velocity time increments in turbulence”. *Phys. Rev. Lett.*, **95**(6), 064501 (2005).
- [13] Choi Y., Lvov Y.V. & Nazarenko S. “Probability densities and preservation of randomness in wave turbulence”. *Phys. Lett. A*, **332**, 230 (2004).
- [14] Cobelli P.J., Maurel A., Pagneux V. & Petitjeans P. “Global measurement of water waves by Fourier transform profilometry”. *Exp. Fluids*, **46**, 1037 (2009).
- [15] Cobelli P.J., Petitjeans P., Maurel A., Pagneux V. & Mordant N.. “Wave turbulence served up on a plate”. *submitted to Phys. Rev. Lett.*
- [16] Connaughton C., Nazarenko S. & Newell A.C. “Dimensional analysis and weak turbulence”. *Physica D*, **184**, 86 (2003).
- [17] Crawford A.M., Mordant N. & Bodenschatz E. “Joint statistics of the Lagrangian acceleration and velocity in fully developed turbulence”. *Phys. Rev. Lett.*, **94**(2), 024501 (2005).
- [18] Crawford A.M., Mordant N., Xu H. & Bodenschatz E. “Fluid acceleration in the bulk of turbulent dilute polymer solutions”. *New J. Physics*, **10**, 123015 (2008).
- [19] During G., Josserand C. & Rica S. “Weak Turbulence for a Vibrating Plate: Can One Hear a Kolmogorov Spectrum?” *Phys. Rev. Lett.*, **97**, 025503 (2006).
- [20] Falcon E., Laroche C. & Fauve S. “Observation of Gravity-Capillary Wave Turbulence”. *Phys. Rev. Lett.*, **98**, 094503 (2007).
- [21] Falkovich G., Gawedzki K. & Vergassola M. “Particles and fields in fluid turbulence”. *Rev. Mod. Phys.*, **73**(4), 913 (2001).

- [22] Frisch U. *Turbulence, the legacy of A. N. Kolmogorov*. Cambridge University Press (1995).
- [23] Gailitis A., Lielausis O., Platacis E., Dementev S., Cifersons A., Gerbeth G., Gundrum T., Stefani F., Christen M. & Will G. “Magnetic field saturation in the Riga dynamo experiment”. *Phys. Rev. Lett.*, **86**, 3024 (2001).
- [24] Gallet B., Berhanu M. & Mordant N.. “Influence of an external magnetic field on forced turbulence in a swirling flow of liquid metal”. *Phys. Fluids* (in press).
- [25] Gissinger C., Iskakov A., Fauve S. & Dormy E. “Effect of magnetic boundary conditions on the dynamo threshold of von Kármán swirling flows”. *EPL*, **82**(2), 29001 (2008).
- [26] Gissinger C.J.P. “A numerical model of the VKS experiment”. *EPL*, **87**(3), 39002 (2009).
- [27] Laguerre R., Nore C., Ribeiro A., Léorat J., Guermond J.L. & Plunian F. “Impact of Impellers on the Axisymmetric Magnetic Mode in the VKS2 Dynamo Experiment”. *Phys. Rev. Lett.*, **101**(10), 104501 (2008).
- [28] Maxey M.R. & Riley J.J. “Equation of motion for a small rigid sphere in a nonuniform flow”. *Phys. Fluids*, **26**, 883 (1983).
- [29] Moffatt H.K. *Magnetic field generation in electrically conducting fluids*. Cambridge University Press (1978).
- [30] Mole N., Schopfloch T.P. & Sullivan P.J. “High concentrations of a passive scalar in turbulent dispersion”. *J. Fluid Mech.*, **604**, 447 (2008).
- [31] Monchaux R., Berhanu M., Aumaitre S., Chiffaudel A., Daviaud F., Dubrulle B., Ravelet F., Fauve S., Mordant N., Pétrélis F., Bourgoin M., Odier P., Pinton J.F., Plihon N. & Volk R. “The von Kármán Sodium experiment: Turbulent dynamical dynamos”. *Phys. Fluids*, **21**, 035108 (2009).
- [32] Monchaux R., Berhanu M., Bourgoin M., Moulin M., Odier P., Pinton J.F., Volk R., Fauve S., Mordant N., Pétrélis F., Chiffaudel A., Daviaud F., Dubrulle B., Gasquet C., Marié L. & Ravelet F. “Generation of a Magnetic Field by Dynamo Action in a Turbulent Flow of Liquid Sodium”. *Phys. Rev. Lett.*, **98**, 044502 (2007).
- [33] Mordant N.. *Mesure lagrangienne en turbulence : mise en œuvre et analyse*. Ph.D. thesis, Ecole Normale Supérieure de Lyon (2001).
- [34] Mordant N.. “Are there waves in wave turbulence ?” *Phys. Rev. Lett.*, **100**(23), 234505 (2008).
- [35] Mordant N.. “Experimental high Reynolds number turbulence with an active grid”. *Am. J. Physics*, **76**(12), 1092 (2008).
- [36] Mordant N., Crawford A.M. & Bodenschatz E. “Experimental Lagrangian acceleration probability density function measurement”. *Physica D*, **193**, 245 (2004).
- [37] Mordant N., Crawford A.M. & Bodenschatz E. “Three-dimensional structure of the Lagrangian acceleration in turbulent flows”. *Phys. Rev. Lett.*, **93**(21), 214501 (2004).
- [38] Mordant N., Delour J., Lévêque E., Arnéodo A. & Pinton J.F. “Long Time Correlations in Lagrangian Dynamics: A Key to Intermittency in Turbulence”. *Phys. Rev. Lett.*, **89**(25), 254502 (2002).
- [39] Mordant N., Lévêque E. & Pinton J.F. “Experimental and numerical study of the Lagrangian dynamics of high Reynolds turbulence”. *New J. Physics*, **6** (2004).
- [40] Mordant N., Metz P., Michel O. & Pinton J.F. “Measurement of Lagrangian Velocity in Fully Developed Turbulence”. *Phys. Rev. Lett.*, **91**, 214501 (2001).
- [41] Mordant N., Metz P., Pinton J.F. & Michel O. “Acoustical technique for Lagrangian velocity measurement”. *Rev. Sci. Instr.*, **76**(2), 025105 (2005).
- [42] Mordant N., Pinton J.F. & Michel O. “Time resolved tracking of a sound scatterer in a complex flow: nonstationary signal analysis and applications”. *J. Acoust. Soc. Am.*, **112**(1), 108 (2002).
- [43] Mordant N., Prada C. & Fink M. “Highly resolved detection and selective focusing in a waveguide using the D.O.R.T. method”. *J. Acoust. Soc. Am.*, **105**(5), 2634 (1999).
- [44] Newell A.C., Nazarenko S. & Biven L. “Wave turbulence and intermittency”. *Physica D*, **152-153**, 520 (2001).
- [45] Ouellette N.T., Xu H. & Bodenschatz E. “Bulk turbulence in dilute polymer solutions”. *J. Fluid Mech.*, **629**, 375 (2009).
- [46] Pétrélis F., Fauve S., Dormy E. & Valet J.P. “Simple Mechanism for Reversals of Earth’s Magnetic Field”. *Phys. Rev. Lett.*, **102**, 144503 (2009).

- [47] Pétrélis F., Mordant N. & Fauve S. “On the magnetic fields generated by experimental dynamos”. *Geo. Astro. Fluid Dyn.*, **101**(3-4), 289 (2007).
- [48] Porta A.L., Voth G.A., Crawford A.M., Alexander J. & Bodenschatz E. “Fluid particle accelerations in fully developed turbulence”. *Nature*, **409**, 1017 (2001).
- [49] Qureshi N.M., Arieta U., Baudet C., Cartellier A., Gagne Y. & Bourgoïn M. “Acceleration statistics of inertial particles in turbulent flow”. *Eur. Phys. J. B*, **66**, 531 (2008).
- [50] Qureshi N.M., Bourgoïn M., Baudet C., Cartellier A. & Gagne Y. “Turbulent Transport of Material Particles: An Experimental Study of Finite Size Effects”. *Phys. Rev. Lett.*, **99**, 184502 (2007).
- [51] Ravelet F., Berhanu M., Monchaux R., Aumaitre S., Chiffaudel A., Daviaud F., Dubrulle B., Bourgoïn M., Odier P., Plihon N., Pinton J.F., Volk R., Fauve S., Mordant N. & Pétrélis F. “Chaotic Dynamos Generated by a Turbulent Flow of Liquid Sodium”. *Phys. Rev. Lett.*, **101**, 074502 (2008).
- [52] Ravelet F., Chiffaudel A., Daviaud F. & Léorat J. “Towards an experimental von Kármán dynamo: Numerical studies for an optimized design”. *Phys. Fluids*, **17**, 117104 (2005).
- [53] Reynolds A.M. “Superstatistical Mechanics of Tracer-Particle Motions in Turbulence”. *Phys. Rev. Lett.*, **91**(8), 084503 (2003).
- [54] Reynolds A.M., Mordant N., Crawford A.M. & Bodenschatz E. “On the distribution of Lagrangian accelerations in turbulent flows”. *New J. Physics*, **7**, 58 (2005).
- [55] Sawford B.L. “Reynolds number effects in Lagrangian stochastic models of turbulent dispersion”. *Phys. Fluids A*, **3**(6), 1577 (1991).
- [56] Sawford B.L. “Turbulent relative dispersion”. *Ann. Rev. Fluid Mech.*, **33**, 289 (2001).
- [57] Stapountzis H., Sawford B.L., Hunt J.C.R. & Britter R.E. “Structure of the temperature field downwind of a line source in grid turbulence”. *J. Fluid Mech.*, **165**, 401 (1986).
- [58] Stefani F., Xu M., Gerbeth G., Ravelet F., Chiffaudel A., Daviaud F. & Léorat J. “Ambivalent effects of added layers on steady kinematic dynamos in cylindrical geometry: application to the VKS experiment”. *Eur. J. Mech. B*, **25**, 894 (2006).
- [59] Stieglitz R. & Müller U. “Experimental demonstration of a homogeneous two-scale dynamo”. *Phys. Fluids*, **13**, 561 (2001).
- [60] Volk R., Calzavarini E., Verhille G., Lohse D., Mordant N., Pinton J.F. & Toschi F. “Acceleration of heavy and light particles in turbulence: comparison between experiments and direct numerical simulation”. *Physica D*, **237**, 2084 (2008).
- [61] Volk R., Mordant N., Verhille G. & Pinton J.F. “Laser Doppler measurement of inertial particle and bubble accelerations in turbulence”. *EPL*, **81**, 34002 (2008).
- [62] Volk R., Ravelet F., Monchaux R., Berhanu M., Chiffaudel A., Daviaud F., Odier P., Pinton J.F., Fauve S., Mordant N. & Pétrélis F. “Transport of magnetic field by a turbulent flow of liquid sodium”. *Phys. Rev. Lett.*, **97**, 074501 (2006).
- [63] Warhaft Z. “The interference of thermal fields from line sources in grid turbulence”. *J. Fluid Mech.*, **144**, 363 (1984).